

Review

Gas Generation in Lithium-Ion Batteries: Mechanisms, Failure Pathways, and Thermal Safety Implications

Tianyu Gong ¹, Xuzhi Duan ¹, Yan Shan ^{1,*} and Lang Huang ^{2,*} 

¹ College of Materials Science and Engineering, Qingdao University of Science and Technology, Qingdao 266101, China; gongty@qibebt.ac.cn (T.G.); duanxz@qibebt.ac.cn (X.D.)

² Qingdao Industrial Energy Storage Research Institute, Qingdao Institute of Bioenergy and Bioprocess Technology, Chinese Academy of Sciences, Qingdao 266101, China

* Correspondence: shanyan@qust.edu.cn (Y.S.); huanglang@qibebt.ac.cn (L.H.)

Abstract: Gas evolution in lithium-ion batteries represents a pivotal yet underaddressed concern, significantly compromising long-term cyclability and safety through complex interfacial dynamics and material degradation across both normal operation and extreme thermal scenarios. While extensive research has focused on isolated gas generation mechanisms in specific components, critical knowledge gaps persist in understanding cross-component interactions and the cascading failure pathways it induced. This review systematically decouples gas generation mechanisms at cathodes (e.g., lattice oxygen-driven CO₂/CO in high-nickel layered oxides), anodes (e.g., stress-triggered solvent reduction in silicon composites), electrolytes (solvent decomposition), and auxiliary materials (binder/separator degradation), while uniquely establishing their synergistic impacts on battery stability. Distinct from prior modular analyses, we emphasize that: (1) emerging systems exhibit fundamentally different gas evolution thermodynamics compared to conventional materials, exemplified by sulfide solid electrolytes releasing H₂S/SO₂ via unique anionic redox pathways; (2) gas crosstalk between components creates compounding risks—retained gases induce electrolyte dry-out and ion transport barriers during cycling, while combustible gas–O₂ mixtures accelerate thermal runaway through chain reactions. This review proposes three key strategies to suppress gas generation: (1) oxygen lattice stabilization via dopant engineering, (2) solvent decomposition mitigation through tailored interphases engineering, and (3) gas-selective adaptive separator development. Furthermore, it establishes a multiscale design framework spanning atomic defect control to pack-level thermal management, providing actionable guidelines for battery engineering. By correlating early gas detection metrics with degradation patterns, the work enables predictive safety systems and standardized protocols, directly guiding the development of reliable high-energy batteries for electric vehicles and grid storage.



Academic Editor: Ivana Hasa

Received: 18 March 2025

Revised: 7 April 2025

Accepted: 10 April 2025

Published: 13 April 2025

Citation: Gong, T.; Duan, X.; Shan, Y.; Huang, L. Gas Generation in Lithium-Ion Batteries: Mechanisms, Failure Pathways, and Thermal Safety Implications. *Batteries* **2025**, *11*, 152. <https://doi.org/10.3390/batteries11040152>

Copyright: © 2025 by the authors. Licensee MDPI, Basel, Switzerland. This article is an open access article distributed under the terms and conditions of the Creative Commons Attribution (CC BY) license (<https://creativecommons.org/licenses/by/4.0/>).

Keywords: gas generation; lithium-ion batteries; thermal runaway; electrochemical cycling; interfacial reactions

1. Introduction

As global energy systems shift towards decarbonization, lithium-ion batteries, which are essential energy storage components for electric vehicles, smart grids, and portable electronics, necessitate concurrent optimization of energy density and safety. High-capacity materials, such as nickel-rich cathodes and silicon-based anodes, enhance energy density, but also intensify cycle life degradation, interfacial side reactions, and thermal runaway risks [1]. Internal gas generation, a universal phenomenon during cycling and thermal

abuse, directly causes capacity fade, impedance surge, swelling, leakage, or even explosion, posing critical safety challenges [2]. The Samsung Galaxy Note 7 recall highlighted the catastrophic risks associated with lithium plating and electrolyte decomposition. Thus, elucidating multi-component gas generation mechanisms and their cross-scale coupling is urgent for material design, failure, and safety protocols [3].

This review synthesizes gas generation pathways and failure mechanisms across cathodes, anodes, electrolytes, and auxiliary materials. Cathode gas behavior correlates with structural stability: layered oxides catalyze electrolyte oxidation via oxygen loss and metal dissolution; spinel materials suffer interfacial side reactions; polyanionic cathodes face metal dissolution-induced decomposition. Anode gas generation stems from SEI dynamics (graphite), volume expansion (Si), and dendrites (Li metal). Gas crosstalk from the cathode to the anode induces corrosion of the anode material, leading to the formation of lithium-ion-insulating salts, such as Li_2O and Li_2CO_3 , at the anode interface. Additionally, shuttling oxygen from the cathode reacts with fresh lithium metal and lithium dendrites at the anode, causing passivation of the anode interface. This triggers severe polarization, reduces cycle life, and even introduces safety risks [4]. The gas species (e.g., H_2 , HF) generated at the lithium battery anode can crosstalk to the cathode through the electrolyte/separator system, accelerating electrolyte decomposition at the cathode interface. This process leads to compromised overall cell performance and elevated thermal runaway risks. Such gas-mediated crosstalk establishes mutual degradation pathways between electrodes, compromising both electrochemical stability and safety. Liquid electrolytes generate gases via solvent/salt reactions, while solid-state electrolyte-based batteries release sulfur- or carbon-based gases due to interfacial incompatibility. Auxiliary materials (binders, conductive agents, residual salts) further complicate gas networks via thermal/chemical decomposition.

Gas generation in lithium-ion batteries systematically deteriorates both cycling performance and thermal stability through mechanisms, spanning material, interfacial, and systemic levels. Regarding cycling performance, gas formation directly depletes electrolytes and active lithium, leading to irreversible capacity fade, while gas accumulation in electrode pores obstructs lithium-ion transport pathways, exacerbating polarization effects. The SEI at the anode undergoes repeated rupture due to mechanical stress from gas buildup, exposing fresh active surfaces and triggering persistent electrolyte decomposition, forming a self-reinforcing degradation cycle. In terms of thermal stability, the accumulation of flammable gases (e.g., H_2 , CO) significantly lowers the thermal runaway initiation temperature. The low thermal conductivity of gases promotes localized heat accumulation, creating hotspots that accelerate chain reactions such as cathode lattice oxygen release and electrolyte oxidative decomposition. Concurrently, mechanical stress from gas accumulation compromises the integrity of the SEI/CEI, exposing reactive surfaces to electrolyte interactions that generate additional heat and gases. These processes establish a “gas generation–heat release–material degradation” positive feedback loop, rapidly driving the battery from normal operation into irreversible thermal runaway.

While material modifications, electrolyte engineering, and *in situ* characterization partially mitigate gas generation, challenges remain in solid-state interface mechanisms, multi-field modeling, and gas-failure threshold quantification [5]. This review integrates multi-scale gas mechanisms, revealing “material–interface–system” failure correlations to guide safer battery design, enabling proactive safety strategies and supporting global carbon neutrality goals.

2. Cathode

In lithium-ion batteries, cathode materials are typically the primary factor limiting the specific capacity of the cell [6]. Currently, the dominant cathode materials encompass

(1) layered materials, such as LiCoO_2 and high-nickel ternary compounds (e.g., NCM); (2) spinel materials, exemplified by LiMn_2O_4 ; and (3) polyanionic materials, including LiFePO_4 . To enhance energy density, high-nickel layered materials and high-voltage-tolerant spinel materials have become the most prominent cathode candidates. However, the pursuit of higher energy density significantly increases the risk of gas generation at the cathode [7]. Among these challenges, lattice oxygen release under high voltage or overheating stands out as one of the most critical issues. At elevated voltages, lattice oxygen loss generates O_2 , which reacts further with the electrolyte, serving as the primary source of substantial gas evolution at the cathode [8,9]. This process accelerates cathode impedance growth, capacity degradation, and safety hazards. This review provides a systematic analysis of gas evolution mechanisms across these three cathode material categories.

2.1. Layered Cathode Materials

Layered cathode materials have attracted considerable research attention. LiCoO_2 -layered cathode materials, which enabled the first successful large-scale commercialization of lithium-ion batteries, marked a new era in battery technology. Their inventor, John B. Goodenough, was awarded the Nobel Prize in Chemistry for this groundbreaking contribution [10]. NCM layered cathodes, characterized by their high specific energy density, are currently the dominant cathode materials for long-range electric vehicles [11]. Nevertheless, gas evolution persists as a major impediment, thereby hindering their further advancement.

In LiCoO_2 cathodes, high-voltage cycling leads to an irreversible phase transition from a layered structure to a spinel-like Co_3O_4 . This structural degradation impedes Li^+ transport, increases impedance, and accelerates capacity fading. Concurrently, lattice oxygen loss generates highly oxidative species such as O_2 and O^- radicals, which rapidly react with electrolyte solvents to produce substantial CO_2 and other gases (Figure 1a) [6]. Thermal abuse testing of NCM/graphite full cells identified gas components, including CO_2 , H_2 , CO , CH_4 , and C_2H_4 (Figure 1b) [12]. Testing of LiCoO_2 -based cells at 90 °C revealed significant gas evolution (primarily CO_2 , CO , and C_2H_4) when the state of charge (SOC) exceeds ~80% during charging (Figure 1c) [13].

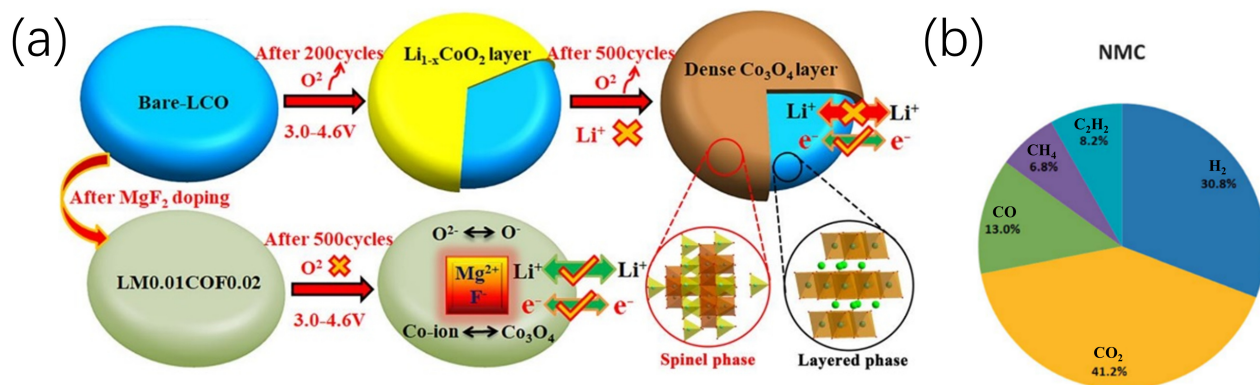


Figure 1. Cont.

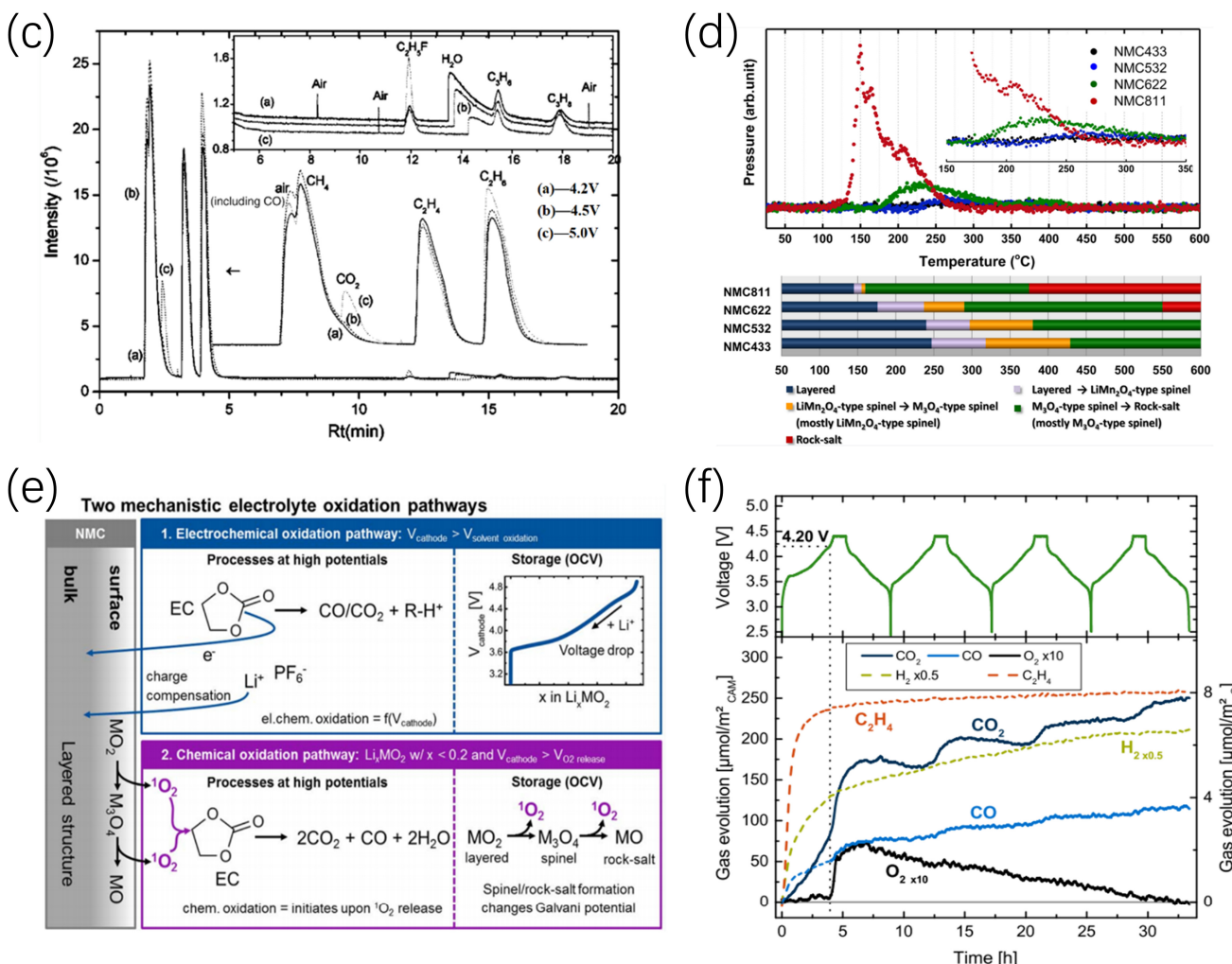


Figure 1. (a) The degradation mechanism schematic diagram of high-voltage LiCoO₂ cathode materials [6]. (b) Components of the produced gases of NMC/graphite cells during the thermal runaway experiments [12]. (c) The gas chromatography of the LiCoO₂ battery under different charging voltages [14]. (d) Mass spectroscopy profiles for the oxygen and the corresponding temperature region of the phase transitions for NMC samples [13]. (e) Schematic description of the proposed electrochemical and chemical electrolyte oxidation pathways (exemplarily shown for EC) which occur at high potentials [15]. (f) Evolution of gas during a high potential (solid lines indicate the gases stemming from the NMC electrode and dashed lines from the graphite electrode) [15].

NCM layered cathodes present similar challenges, especially at elevated temperatures and high voltages. At high temperatures, NCM materials decompose, releasing O₂, with significant CO₂ generation detected at the cathode side [16]. As shown in Figure 1d, higher nickel content correlates with lower thermal decomposition onset temperatures and greater oxygen release. For example, NCM433 initiates decomposition at 245 °C, whereas NCM811 begins at 135 °C [13]. Under high-voltage conditions, NCM cathodes predominantly generate CO₂ and CO via chemical reactions between reactive lattice oxygen and electrolytes, rather than direct electrochemical decomposition of electrolytes (Figure 1e). High-voltage cycling induces sequential phase transitions from layered to disordered spinel and ultimately rock salt structures at the cathode surface, accompanied by lattice oxygen release and impedance rise (Figure 1f) [15].

For all NCM materials, singlet oxygen (${}^1\text{O}_2$) evolution initiates when SOC exceeds 80%, independent of electrode potential but dependent on lithium extraction levels. Elevated nickel content amplifies oxygen evolution rates and diminishes its onset potential,

attributable to higher SOC values at equivalent voltages [17]. Lattice oxygen loss not only drives gas evolution, but also severely degrades capacity, with 1% oxygen loss causing up to 21% capacity fade [18]. Reactions between lattice oxygen and electrolytes predominantly occur at NCM surfaces, with activity governed by nickel content and delithiation degree. Increased nickel content enhances surface reactivity and destabilizes lattice oxygen, while deeper delithiation elevates Ni^{4+} concentrations. Investigations into lithium-excess NCM cathodes have revealed higher Ni^{4+} content compared to conventional materials, leading to accelerated O_2 and CO_2 generation during cycling. Higher delithiation levels further reduce the onset temperature for gas evolution and structural degradation while accelerating gas production rates (Figure 2) [18,19]. In summary, gas evolution in layered cathodes primarily originates from lattice oxygen–electrolyte reactions under high-temperature and high-voltage conditions. While increasing nickel content enhances energy density, it significantly compromises structural stability, exacerbates lattice oxygen loss, accelerates impedance growth, and intensifies capacity degradation, ultimately undermining cycle life and safety. Therefore, enhancing lattice oxygen stability represents a critical challenge in developing high-energy-density layered cathode materials.

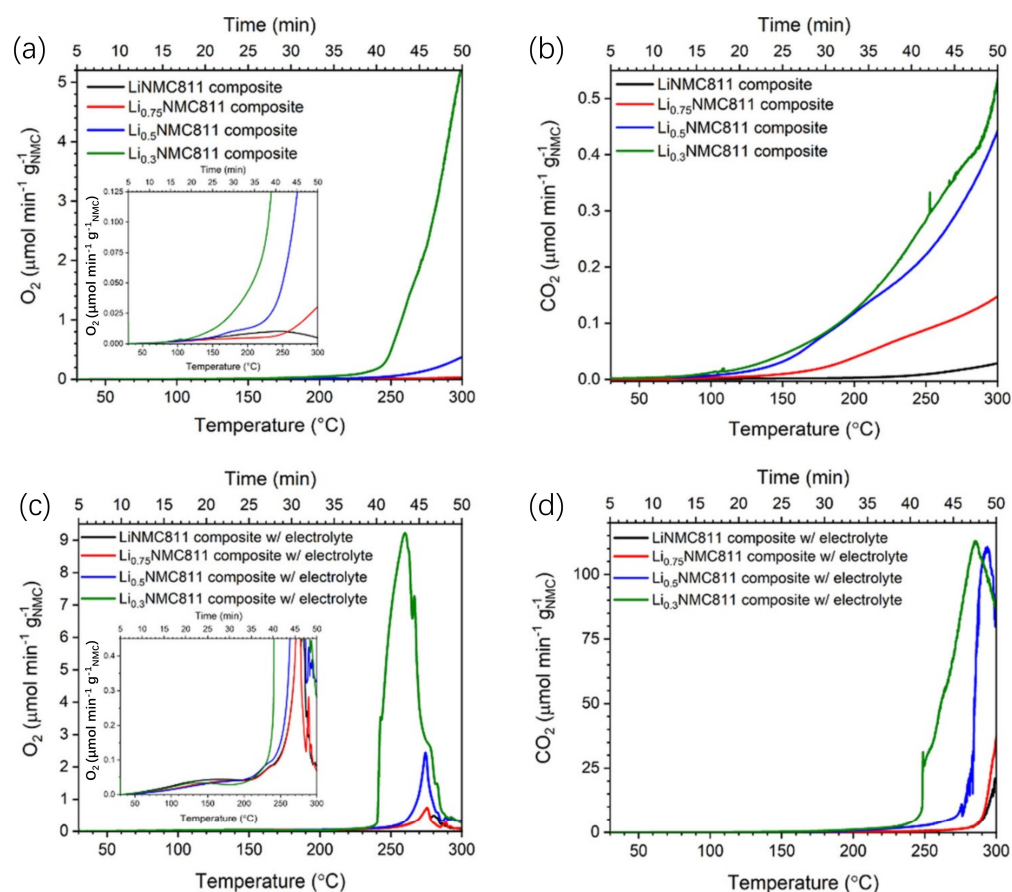


Figure 2. During heating from room temperature to 300 °C, (a) O_2 and (b) CO_2 release of NMC811 composites without the presence of an electrolyte. (c) O_2 and (d) CO_2 release of NMC811 composites with the presence of an electrolyte [19].

2.2. Spinel Cathode Materials

Spinel LiMn_2O_4 (LMO) exhibits advantages, including high electronic conductivity, low cost, superior structural stability compared to layered counterparts, and high-voltage operation capability [20]. Among these materials, $\text{LiNi}_{0.5}\text{Mn}_{1.5}\text{O}_4$ (LNMO) spinel stands out as a promising high specific energy cathode due to its high theoretical capacity (147 mAh g^{-1}) and elevated operating voltage (4.7 V vs. Li/Li^+) [21].

Overcharge testing of LMO-based cells reveals gas evolution profiles analogous to LCO systems, yet with the additional generation of C_2H_2 , their concentration increases with the applied voltage. As shown in Figure 3, the higher lattice oxygen stability of LMO compared to LCO inhibits C_2H_2 oxidation by O_2 , leading to its accumulation [14]. Roland Jung et al. demonstrated the superior stability of spinel materials under overcharge conditions: while NCM cathodes generate substantial CO and CO_2 below 4.8 V, LNMO cathodes maintain minimal gas evolution, even at 5.0 V [15]. As illustrated in Figure 3, GC analysis revealed the relative proportions of gaseous products extracted from the cells. Consistent with prior observations, elevated testing temperatures correlated with increased gas evolution: the cell subjected to 60 °C exhibited the highest gas volume, followed by the 45 °C cell, and finally the 30 °C cell [22]. Hydrogen constituted the predominant gas species across all samples; however, its relative abundance decreased progressively with increasing temperature. Additionally, CO, CO_2 , and hydrocarbon compounds detected in the gaseous mixture were indicative of electrolyte decomposition processes. Thermal abuse testing of LMO/graphite full cells produces CO_2 -dominated gas mixtures with minor CO and hydrocarbons, accompanied by toxic species (HF , SO_2 , HCl , NO), with gas emission rates accelerating at higher SOC (Figure 3) [23]. Comparative thermal runaway studies show that LMO cells generate approximately twice the CO volume of NCM counterparts [24]. Transition metal dissolution in LMO electrodes further drives gas evolution. Trace H^+ triggers Mn^{3+} disproportionation, yielding Mn^{2+} and Mn^{4+} . The leached Mn^{2+} migrates and deposits on the anode, where it catalyzes irreversible side reactions that degrade the SEI layer, promote inorganic component formation, and induce continuous electrolyte reduction with persistent gas evolution [25]. Mn deposition predominantly occurs near the separator-facing graphite surface, with MnO and MnO_2 identified within thickened SEI layers, indicative of enhanced electrolyte decomposition [26,27] (Figure 3). Although LMO cathodes exhibit superior lattice oxygen stability under high voltages, continuous Mn dissolution during cycling causes cumulative electrolyte depletion and gas generation, severely degrading cycling stability and safety. This intrinsic limitation constitutes a major barrier to the large-scale commercialization of LMO-based systems.

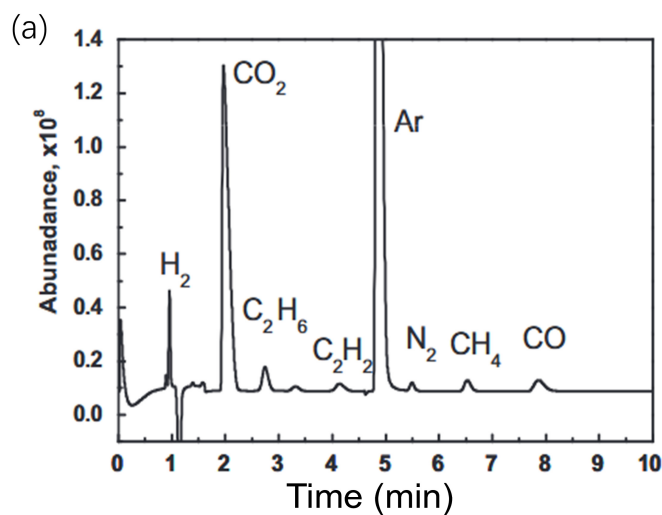


Figure 3. Cont.

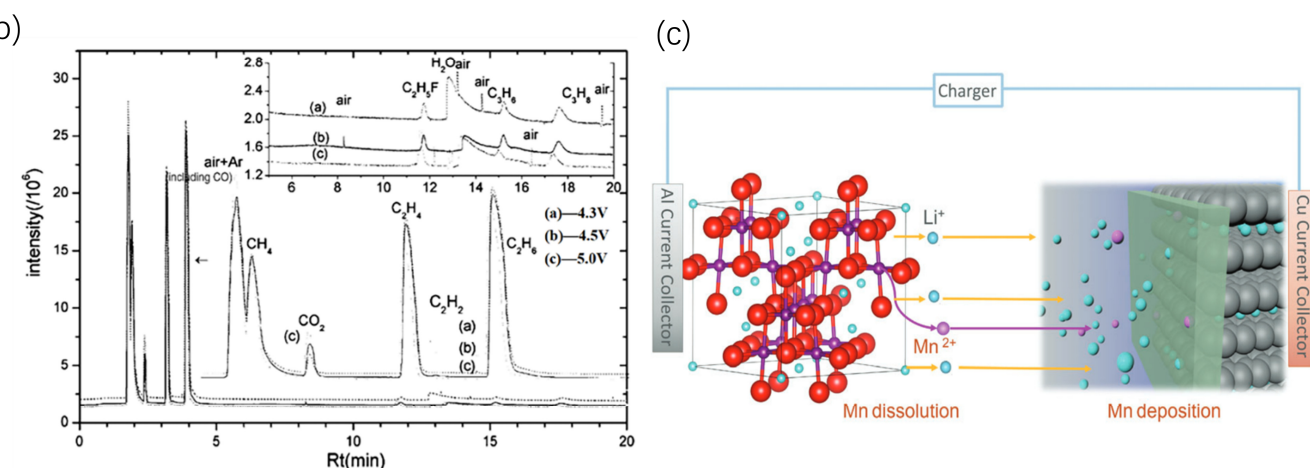


Figure 3. (a) Gas chromatography (GC) test results of the Gr/LMO pouch cell after discharge to 1.0 mV [23]. (b) The gas chromatography of the CMS/LiMn₂O₄ battery under different charging voltages [14]. (c) Mn²⁺ deposits on the anode and damages the SEI.

2.3. Polyionic Cathode Materials

A representative example of polyionic cathode materials is LiFePO₄ (LFP). Despite its relatively low energy density and poor electronic conductivity, LFP exhibits exceptional thermal stability, cycling performance, and safety, making it the safest among the three major cathode materials and widely adopted in various applications [28]. Under overcharge conditions, LFP demonstrates the highest lattice oxygen stability compared to NCM and LMO cathodes (Figure 4a), with limited oxidative capability during delithiation, resulting in insufficient oxygen release to react with electrolytes and generate CO₂. As shown in Figure 4, instead, electrolyte decomposition predominantly yields hydrocarbon compounds [14]. Overcharge testing of LFP cells reveals gas evolution, including CO₂, H₂, C₂H₄, CO, and C₂H₂F, with significant gas release initiating at ~120% SOC (Figure 4b). At 130% SOC, substantial gas evolution occurs, accompanied by a temperature rise to ~140 °C, followed by HF generation during cooling [29]. Although LFP exhibits excellent thermal stability, lattice oxygen loss still occurs under heating, producing significant amounts of CO₂, H₂, and CO. Gas evolution is largely independent of SOC, but higher SOC values correlate with increased flammable gas generation. Among the three cathode materials, LFP exhibits the highest gas evolution onset temperature and the lowest gas volume, underscoring its superior safety [12,30]. Overall, LFP's exceptional stability and safety minimize gas evolution impacts under both high-temperature and high-voltage conditions. A 23 Ah commercial LFP battery was placed in a sealed chamber to trigger TR. The temperature and pressure characteristics of the gas within the sealed chamber during this process are shown in Figure 4c. As shown in Figure 4d, the STA-MS test results for a single cathode indicate no O₂ release below 600 °C. Additionally, the exothermic reaction occurring after 500 °C correlates with the generation of CO₂, which is likely caused by a chemical reaction between the cathode and the graphite coating on its surface.

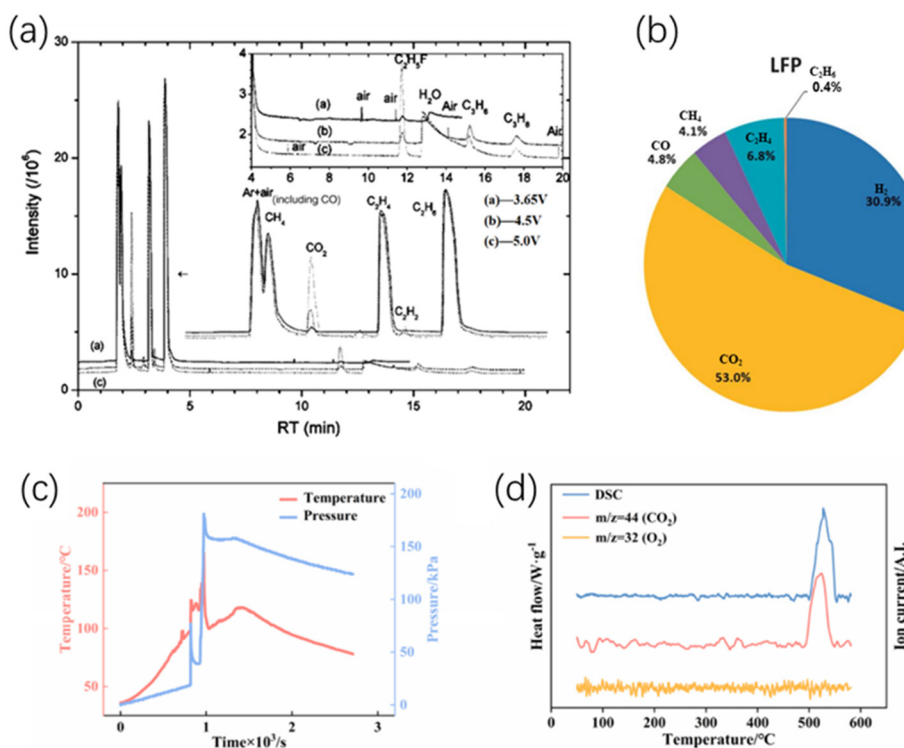


Figure 4. (a) The gas chromatography of the LiMn_2O_4 battery under different charging voltages [14]. (b) Components of the produced gases of LFO/graphite cells during the thermal runaway experiments [12]. (c) Closed container temperature and pressure characteristics of LFP batteries during TR [31]. (d) STA-MS curves of LFP battery cathode [31].

2.4. Cathode Gas–Thermal Runaway Coupling

Gas generation mechanisms are fundamentally associated with thermal runaway in cathode materials. Layered cathodes exhibit oxygen release at elevated temperatures, which subsequently reacts with the electrolyte, generating flammable gases (e.g., ethylene, CO) and significant heat, thereby accelerating battery temperature escalation. In polyanionic cathode systems, combustible gases from electrolyte decomposition ignite upon reaching concentration thresholds under residual active oxygen or transition metal catalysis, triggering intense combustion. High-nickel cathodes, in particular, release fluorine-containing gases (e.g., HF) through reactions between residual lithium compounds and binders at elevated temperatures, leading to interfacial corrosion and accelerating thermal runaway. Below 250 °C, thermal failure species remain largely unchanged; however, above 250 °C, significant HF, fluoroalkanes (e.g., $\text{C}_2\text{H}_5\text{F}$), and ethers (e.g., dimethyl ether) are generated due to oxygen release from NCM cathodes. This oxygen oxidizes EC/EMC solvents to form CO_2 and H_2O , while H_2O vapor triggers LiPF_6 hydrolysis, producing HF. Reactive HF further reacts with C_xH_y to form fluoroalkanes and induces transition metal dissolution from cathodes, exacerbating electrolyte decomposition into ethers. Although partial alcohols oxidize to aldehydes (e.g., CH_3CHO), the observed organic byproducts (alcohols, esters, aldehydes) are minimal, likely due to oxidation or combustion under high oxygen levels at elevated temperatures, ultimately converting to CO_2 and H_2O . These gas-phase reactions, coupled with heat release and interfacial corrosion, establish a self-sustaining cycle that drives thermal runaway propagation (Figure 5) [32]. LFP batteries exhibit superior thermal stability and the slowest pressure build-up within the battery (Figure 6) [33].

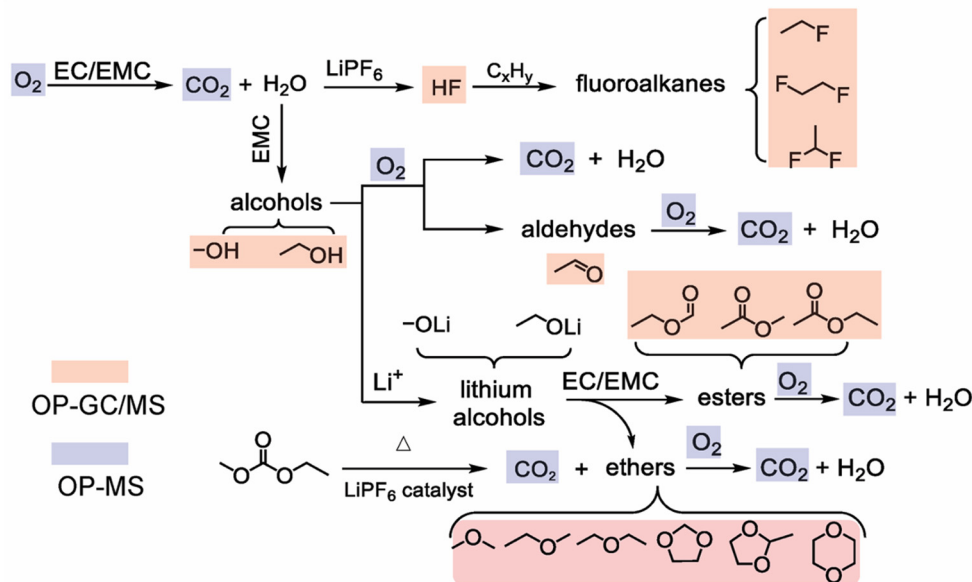


Figure 5. Proposed thermal failure mechanism/pathways on NCM cathode side. The blue region marks the gaseous species detected by OP-MS and the pink region marks the gaseous species detected by OP-GC/MS. The electrolyte and its thermal decomposition products continue to react with the released O₂ on NCM cathode side during the heating process [32].

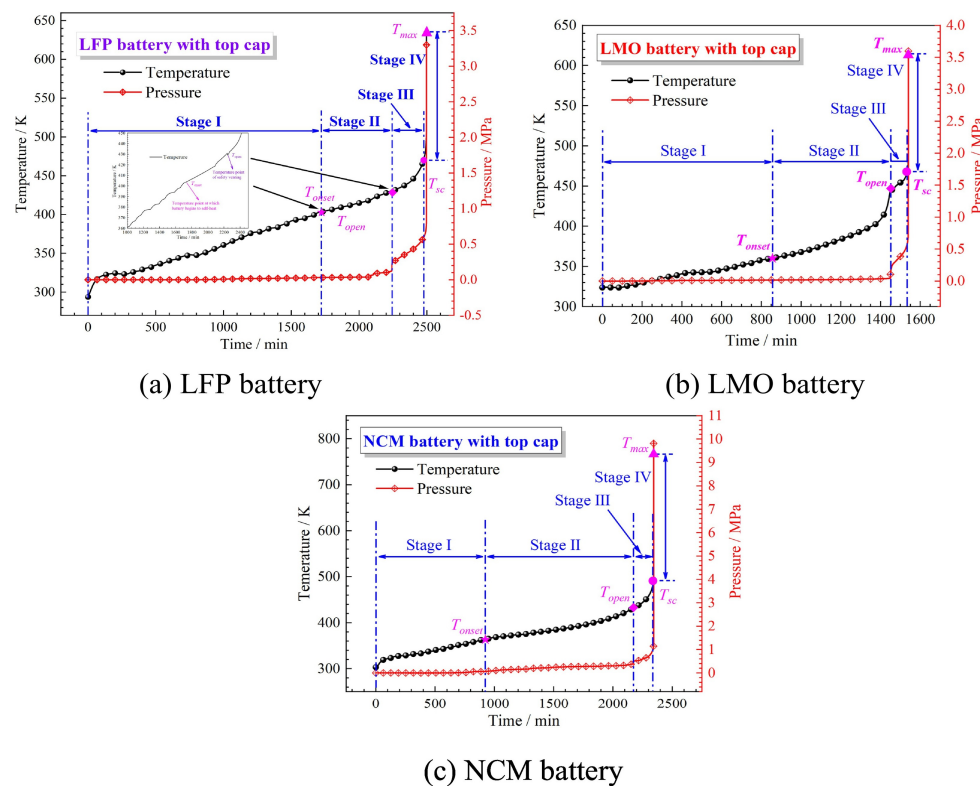


Figure 6. Temperature and pressure versus time curves for flexible pack cells with three different cathodes [33].

The gas evolution (e.g., CO₂, O₂, CO) during cycling of lithium-ion battery cathode materials critically affects battery performance and safety. Layered cathode materials are prone to lattice oxygen loss and oxygen release under high voltage or high SOC, accompanied by transition metal ion dissolution. These processes accelerate electrolyte oxidative decomposition, leading to a thickened CEI, impeded lithium-ion transport, and subsequent

capacity degradation. Additionally, acidic substances formed by the reaction of oxygen with the electrolyte further corrode the electrode, forming unstable interfacial structures that increase internal resistance and reduce cycle life. In contrast, polyanionic cathodes (e.g., LiFePO₄) exhibit higher structural stability. However, under high temperatures or overcharging conditions, metal ion dissolution may still catalyze electrolyte decomposition, producing gases such as CO₂ and HF, resulting in electrolyte depletion and electrode surface passivation. Gas accumulation directly induces the mechanical deformation of the battery, increasing internal pressure and causing cell swelling, separator–electrode delamination, and disruption of uniform lithium-ion diffusion paths. Gas trapped in electrode pores can form localized “dead zones”, exacerbating the decline in active material utilization.

In lithium-ion batteries, the crosstalk from cathode gas generation to the anode primarily originates from the structural instability of cathode materials under high voltage or elevated temperatures and the oxidative reactions of the electrolyte. Cathode materials, particularly nickel-rich layered oxides (e.g., NCM811) and lithium-rich layered oxides, undergo irreversible phase transitions during charging, leading to the release of lattice oxygen. These oxygen species (e.g., O₂, O₂²⁻, O²⁻) exhibit high reactivity and react with organic carbonate solvents in the electrolyte through oxidation, generating gases such as CO₂ and CO. These gases diffuse through the separator to the anode, triggering side reactions that result in thickening of the SEI and increased impedance, thereby accelerating capacity fading. Additionally, the dissolution and migration of transition metal ions (e.g., Mn²⁺, Ni²⁺, Co²⁺) from the cathode into the electrolyte constitute another critical mechanism of cathode-to-anode crosstalk. These metal ions migrate via the electrolyte to the anode surface, where they deposit and destabilize the SEI, resulting in the growth of lithium dendrites and rapid battery failure (Figure 7) [34].

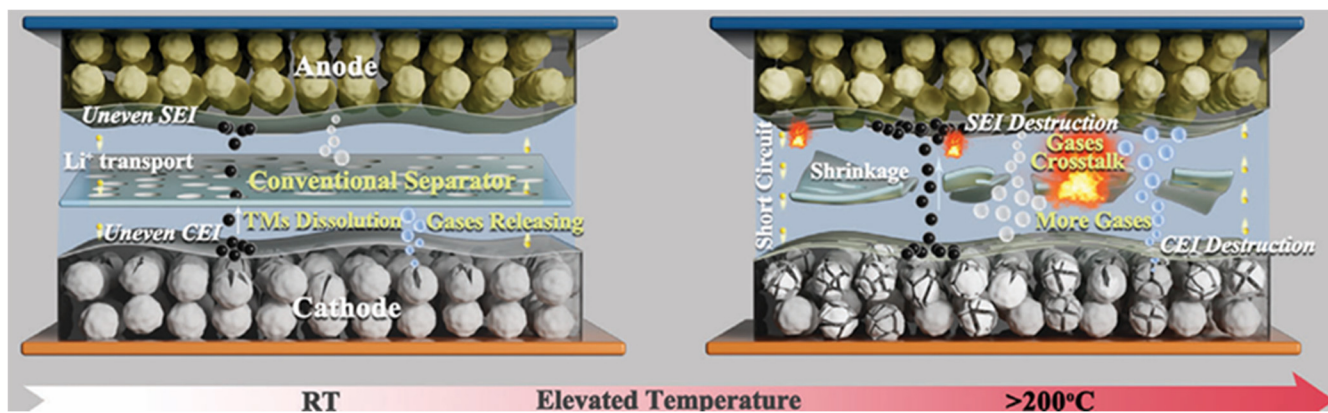


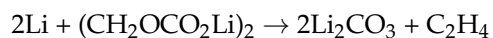
Figure 7. Schematic diagram of thermal runaway induced by gas crosstalk in commercially available batteries [34].

3. Anode Materials

In lithium-ion batteries, gas generation at the anode is the primary source of gas evolution, particularly during the initial cycling process. During the first charge–discharge cycle, the electrolyte reacts with active lithium to form a SEI, generating significant gas at the electrode/electrolyte interface [35–37]. The SEI is a nanoscale passivation layer that is electronically insulating yet ionically conductive, protecting the anode from further electrolyte reactions [38]. The SEI decomposes exothermically at 90–120 °C, with metastable components such as (CH₂OCO₂Li)₂ decomposing to produce C₂H₄, CO₂, and O₂ via the reaction:



Alternatively, it reacts with Li to generate C₂H₄:



At higher temperatures, inorganic Li₂CO₃ decomposes to release CO₂ [39,40]. Volume expansion during cycling can also cause SEI cracking, exposing active lithium to the electrolyte and triggering further gas evolution [41]. Gas generation at the anode is thus closely linked to SEI formation, decomposition, and mechanical failure. Below, gas evolution behaviors in the four following anode materials are examined: graphite, silicon, lithium metal, and lithium titanate.

3.1. Graphite Anode

Graphite is the predominant anode material owing to its cost-effectiveness, structural robustness, low operating potential, and high specific capacity [42]. As shown in Figure 8a, during initial cycling, graphite anodes generate significant C₂H₄ gas, along with minor H₂ and CO, but no CO₂ is detected via in situ infrared spectroscopy [43]. Gas generation is primarily attributed to SEI formation, which stabilizes after initial cycles, halting further gas evolution. Trace water content within the electrolyte can induce additional H₂ and CO₂ generation, with elevated water concentrations increasing H₂ production while suppressing C₂H₄ formation. Stable SEI formation during cycling suppresses water decomposition. Initial cycles also produce minor CO₂, which is consumed over time, likely due to OH⁻ generation from water electrolysis triggering EC decomposition [44]. The simultaneous maximum rates of H₂ generation and CO₂ consumption suggest a reaction between CO₂ and OH⁻ (Figure 8b) [45]. Barbara Michalak et al. also observed a correlation between H₂ and CO₂ generation [46]. As shown in Figure 8c, adding vinylene carbonate (VC) forms a protective SEI layer, reducing H₂ evolution to 13% of its original level. VC additives also reduce ethylene release by 60% but generate CO₂ as a byproduct [47]. Under high-temperature and overcharge conditions, graphite anodes produce more H₂, sourced not only from water but also from electrolyte oxidation at the cathode, with enhanced H₂ generation due to crosstalk between electrodes [48,49]. At low temperatures, increased electrolyte viscosity and reduced conductivity slow charge transfer kinetics, leading to lithium plating on the anode surface instead of intercalation into graphite. Lithium plating damages the SEI, causing its regeneration and thickening, or forms a secondary SEI on the surface. The highly reactive plated lithium reacts violently with the electrolyte, generating significant gas and lithium dendrites, severely compromising capacity and safety [50,51]. Ethyl acetate (EA) exhibits excellent low-temperature performance as a solvent. In 1.0M LiPF₆ EA/FEC electrolyte, gas evolution at −20 °C far exceeds that at 45 °C due to the inability of plated Li to passivate, resulting in vigorous reactions between EA and Li to form H₂ and alkanes [48]. Constructing a stable SEI is the primary method to suppress gas evolution in graphite anodes. However, effective strategies to mitigate low-temperature gas generation remain elusive, making it a key focus for future graphite anode development.

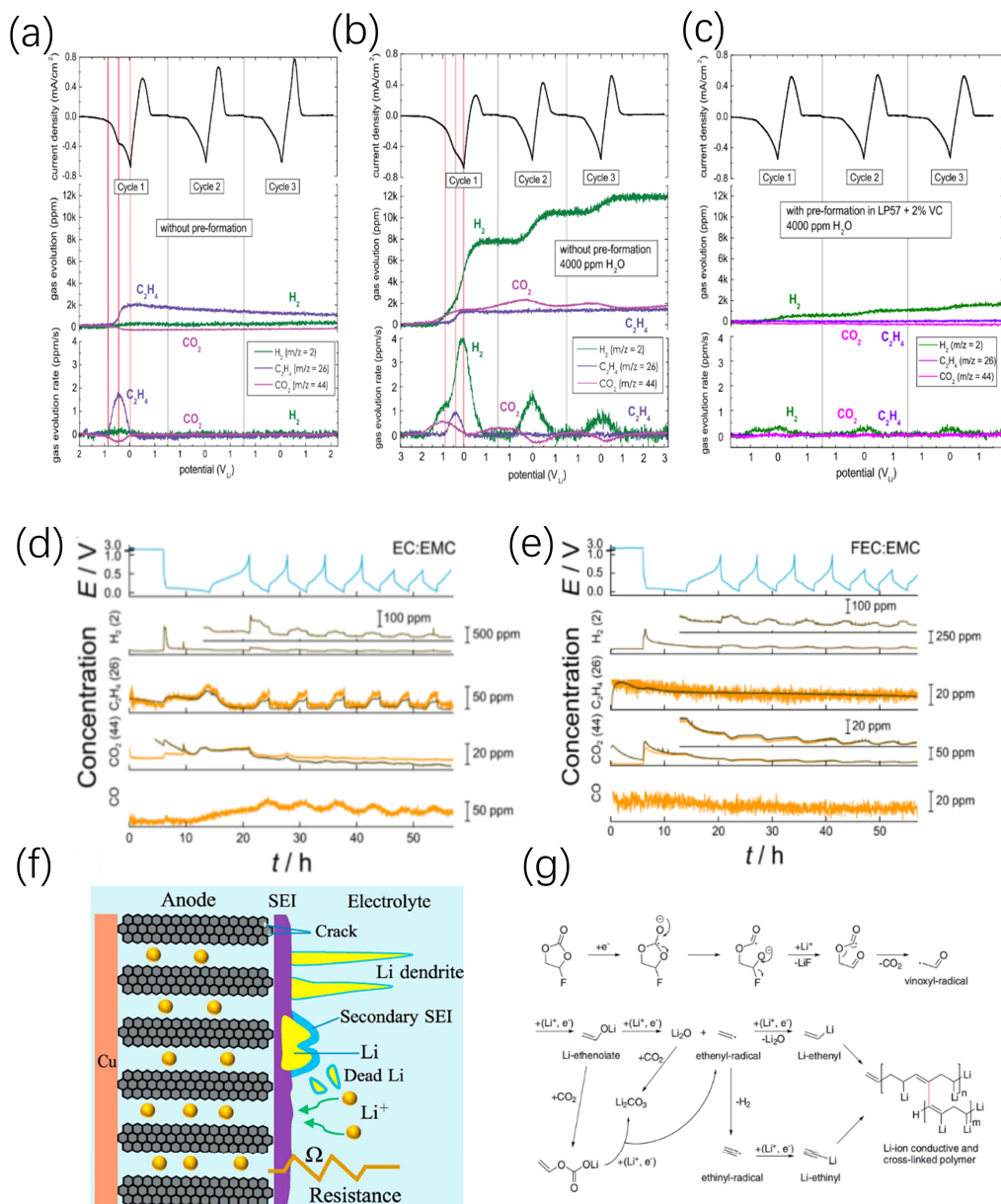


Figure 8. (a) Gas evolution during the first three formation cycles of a pristine graphite working-electrode vs. a metallic lithium counter-electrode in EC/EMC (<20 ppm H₂O) [45]. (b) Gas evolution during the first three formation cycles of a pristine graphite working electrode vs. a metallic lithium counter-electrode in EC/EMC(4000 ppm H₂O) [45]. (c) Gas evolution during three cycles of a pre-cycled graphite working electrode vs. a metallic lithium counter-electrode in EC/EMC containing 4000 ppm H₂O. Pre-formation is performed with 10 galvanostatic charge/discharge cycles at C/10 in EC/EMC + 2% VC (<20 ppm H₂O) [45]. The gas evolution for the first seven cycles of Si half-cells in (d) EC:EMC and (e) FEC:EMC [3]. (f) The degradation mechanism caused by lithium plating on anode under low temperature [52]. (g) Proposed mechanism for the reductive decomposition of FEC [53].

3.2. Silicon Anode

Silicon is a compelling anode material, boasting a theoretical capacity and order of magnitude greater than graphite, coupled with abundant resources and manageable costs, positioning it as a prime candidate to supplant graphite and enhance lithium-ion battery energy density [54]. The resultant instability of the SEI on silicon anodes leads to cracking during cycling, triggering continuous electrolyte reactions with the active material, gas evolution, and capacity fade, thereby posing considerable safety concerns [55,56]. In silicon

anode cells, Si and Li alloy at low potentials, while electrolyte components decompose on the anode surface to form the SEI and generate gases. Unlike graphite anodes, which primarily use EC as the electrolyte solvent, silicon anodes predominantly produce H₂, C₂H₄, and CO due to SEI instability. Fluorinated ethylene carbonate (FEC) is commonly used as a solvent or additive in silicon anode cells to form a more stable SEI, improve Coulombic efficiency, and reduce gas evolution. As shown in Figure 8d,e, when FEC replaces EC, the primary gas components are H₂ and CO₂, with H₂ generated during initial cycles due to trace water and CO₂ from FEC decomposition [3].

When FEC is used as an additive, it undergoes preferential decomposition over EC, with EC decomposition only commencing after complete FEC consumption. SEI cracking due to silicon volume expansion during cycling continuously consumes FEC, generating CO₂ (Figure 8f). They proposed a new FEC reduction mechanism: each FEC molecule consumes four electrons to produce CO₂, LiF, Li₂O, Li₂CO₃, H₂, and crosslinked polymers (Figure 8g) [53]. Addressing SEI cracking caused by volume expansion is the primary research direction for mitigating gas evolution in silicon anodes.

3.3. Lithium Metal Anode

Lithium metal anodes offer ultra-low redox potentials and ultra-high theoretical capacities, thereby holding considerable promise for augmenting battery energy density [57]. Unfortunately, lithium metal is highly reactive and reacts with all known electrolytes. Lithium metal batteries generate significant gases, including CH₄, CO, CO₂, O₂, C₂H₆, H₂, C₂H₄, C₃H₆, C₃H₈, C₄H₈, and C₄H₁₀, with flammable CH₄ and CO accounting for 93% of the total (Figure 9a,b). Ion–solvent complexes decompose more readily on lithium metal anodes [58]. Volume expansion and dendrite growth during cycling cause repeated SEI breakdown and reformation, continuously consuming the electrolyte and generating gases [59]. Lithium metal anodes produce significant H₂, which is greatly reduced when replaced with LiFeO₂. As shown in Figure 9c,d, trace water in the electrolyte is not the primary source of H₂; instead, protonated solvents oxidized at the cathode are reduced to H₂ at the anode. Open-circuit storage also generates substantial H₂ and CO₂, with higher gas volumes than during normal cycling [60].

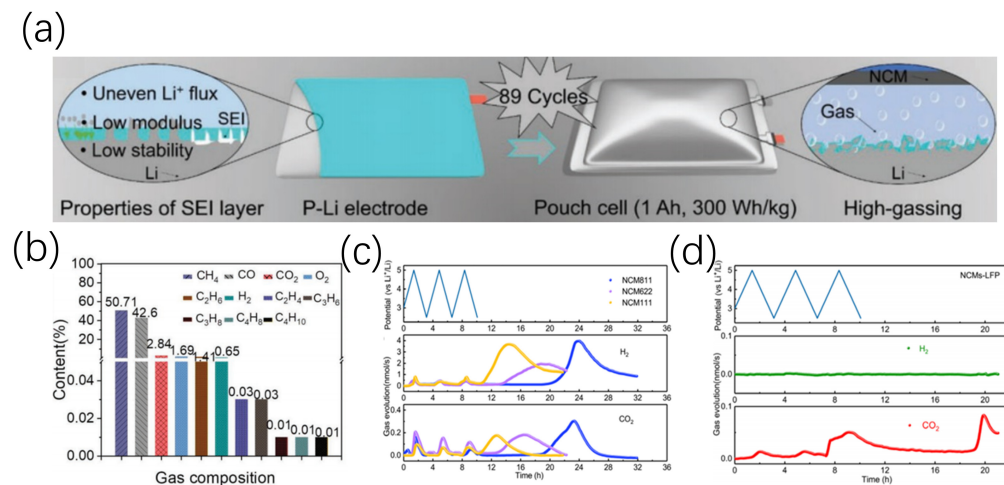


Figure 9. Cont.

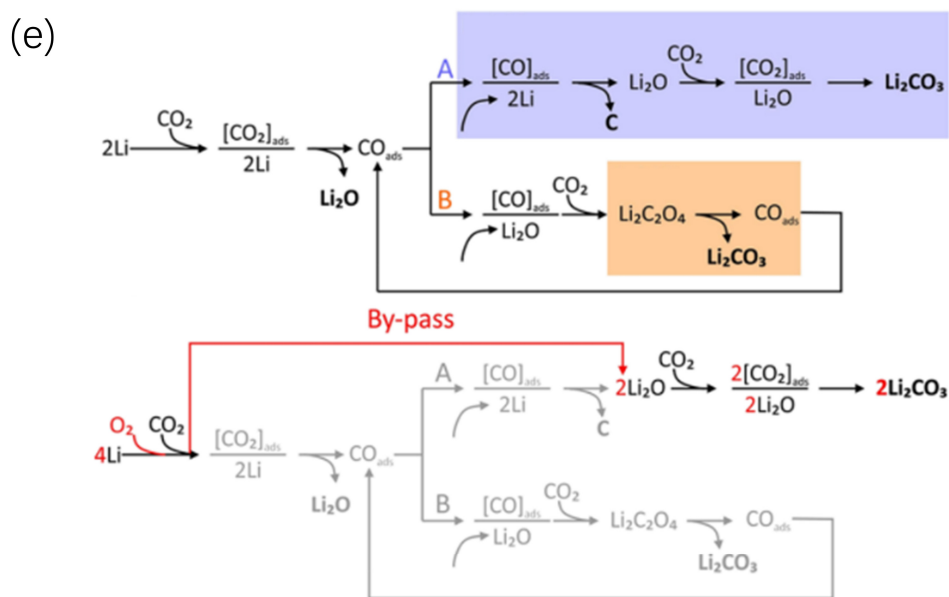
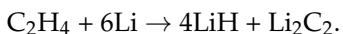


Figure 9. (a) Schematic illustrations of Li electrode structures in the high-energy Li metal pouch cells. (b) Type and content of gases produced in the Li/NCM523 pouch cell [58]. (c) In situ gaseous evolution rate for the NCMs-Li cells over three charge/discharge cycles, (d) In situ gaseous evolution rate for the NCM-LFP cells over three charge/discharge cycles [60]. (e) Pathway of the reaction of CO_2 gas with the Li metal surface; pathway of the reaction of CO_2 and O_2 gases with the Li metal surface [61].

Gas evolution adversely affects lithium deposition morphology, leading to uneven deposition, dendrite growth, and dead lithium formation, severely impacting capacity and safety [62]. Lithium metal also reacts with gas species. For example, EC decomposition produces ethylene, which reacts with lithium to form LiH and Li_2C_2 [12]:



Li_2C_2 in the SEI's inner layer exhibits slower lithium diffusion and higher electronic conductivity than other inorganic components like Li_2O and Li_2CO_3 , increasing interfacial impedance and degrading performance [63]. As shown in Figure 9e, lithium also reacts with CO_2 to form lithium oxalate and carbonate intermediates, releasing CO. In the presence of O_2 , lithium carbonate forms directly [61]. These factors contribute to severe capacity fading and gas generation in lithium metal batteries, hindering their commercialization.

3.4. Anode Gas-Thermal Runaway Coupling

During thermal runaway, anode-generated gases exacerbate the process through dual mechanisms: (1) elevated temperatures ($>80^\circ\text{C}$) induce SEI decomposition, releasing heat and flammable gases (e.g., H_2), which subsequently form explosive mixtures with cathode-derived oxygen; (2) lithium dendrite melting under thermal accumulation triggers internal short circuits, leading to instantaneous heat release, electrolyte vaporization, and rapid internal pressure rise. Notably, silicon-based anodes exhibit accelerated gas generation during early thermal runaway due to exothermic Si-Li alloy reactions ($\Delta H > 1500 \text{ J/g}$), where released H_2 reacts with electrolyte decomposition products (e.g., PF_5) to form toxic gases (e.g., HPF_6), further complicating the reaction chain. Gas analysis reveals significant quantities of CH_3CHO , 2-methyl-1,3-dioxolane, HF, alcohols, esters, and ethers at 100°C , primarily attributed to residual electrochemical reduction products in the electrolyte. As temperatures rise, LiPF_6 hydrolysis generates HF, while PVDF binder

pyrolysis releases fluorine-containing gases (e.g., HF, C_xH_yFz). HF reacts with SEI carbonate components to produce CO_2 and with hydrocarbons to form fluoroalkanes (e.g., C_2H_5F). Concurrently, $LiPF_6$ -catalyzed thermal decomposition of EMC solvent yields CO_2 and ethers (e.g., dimethyl ether), while alcohols (e.g., CH_3OH , C_2H_5OH) combine with Li^+ to form lithium alkoxides, which nucleophilically attack EC/EMC, generating esters and ethers. Proton sources (e.g., HF, H_2O) react with LiC_x/Li to release H_2 , which is detected via OP-MS, with these exothermic reactions collectively driving heat accumulation and pressure buildup, intensifying thermal runaway propagation (Figure 10) [32].

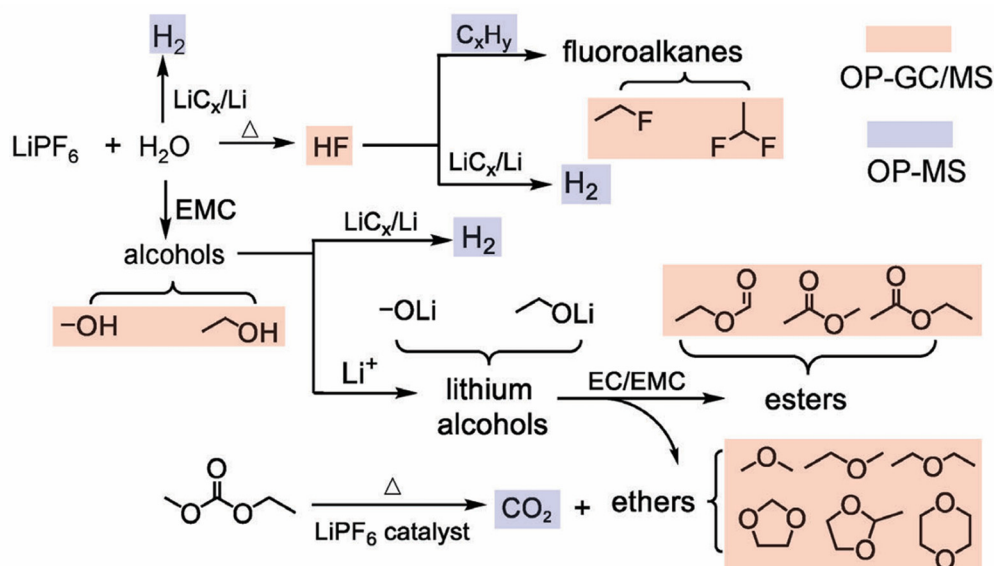


Figure 10. Proposed thermal failure mechanism/pathways on LiC_x anode side. The blue region marks the gaseous species detected by OP-MS and the pink region marks the gaseous species detected by OP-GC/MS. During heating process, the carbon-based electrolyte (containing trace contaminants and cycling products) would tend to decompose thermally and decomposition products would continue to react with the Li/LiC_x anode [32].

Gas generation in lithium-ion battery anodes is primarily driven by electrolyte reduction, the dynamic evolution of the SEI, and lithium dendrite growth. The produced gases (e.g., H₂, CH₄, C₂H₄) critically influence cycle life, failure modes, and thermal runaway risks. During cycling, repeated SEI fracture and reformation on graphite anodes lead to continuous electrolyte reduction (e.g., EC decomposition into H₂ and CO). Silicon-based anodes suffer from severe volume expansion (>300%), exacerbating electrode cracking and fresh surface exposure, further promoting gas generation. Gas accumulation within pores or interfaces impedes lithium-ion diffusion and elevates interfacial impedance, leading to accelerated capacity fade (e.g., silicon–carbon anodes often exhibit <70% capacity retention after 100 cycles). Additionally, lithium plating on anode surfaces catalyzes electrolyte decomposition into flammable alkanes (e.g., C₂H₄), induces uneven current distribution, and accelerates “dead lithium” formation and active lithium loss. Regarding failure mechanisms, gas-induced mechanical stress leads to electrode pulverization or current collector detachment, causing electrical contact failure. Small molecules like H₂ may migrate through the separator to the cathode under high pressure, reacting with high-valence cathode materials (e.g., NCM) to exacerbate transition metal dissolution and electrolyte depletion.

The crosstalk from anode gas generation to the cathode primarily stems from the reduction reactions of the electrolyte during charge–discharge cycles and gas generation under thermal runaway conditions. During initial cycling, SEI formation on the anode surface is accompanied by reductive gas generation, such as H₂ and C₂H₄. These gases

diffuse through the separator to the cathode, where they react with the cathode material, leading to surface passivation of the cathode and dissolution of transition metal ions, thereby accelerating capacity fading. Particularly under high-temperature or overcharging conditions, the thermal decomposition of the anode SEI generates a significant amount of reductive gases (e.g., H_2 , CH_4 , C_2H_4), which diffuse through the separator to the cathode and undergo intense exothermic reactions with oxygen species released from the cathode, triggering thermal runaway. Research indicates that the stability of the SEI on the anode material, the composition of the electrolyte, and the design of the separator are critical for suppressing the crosstalk from anode gas generation to the cathode. By optimizing the structure of the SEI, employing functional electrolyte additives, and designing separators with selective ion transport capabilities, the crosstalk from anode gas generation to the cathode can be effectively mitigated, thereby enhancing the safety and cycle life of the battery (Figure 11) [64].

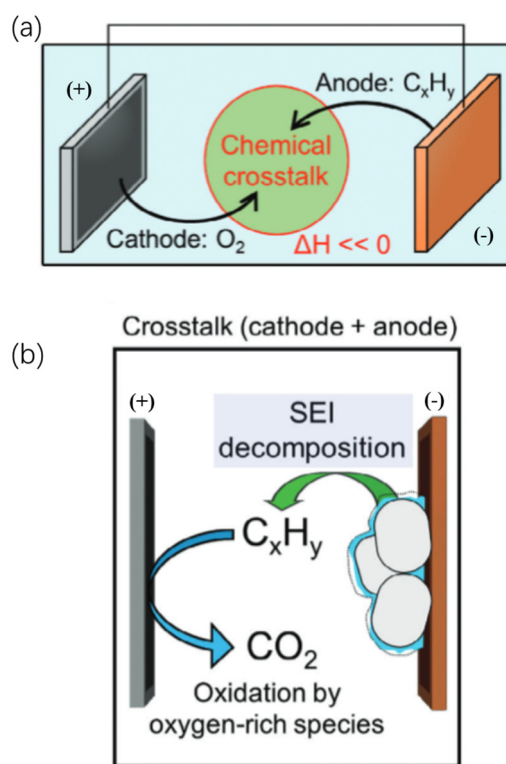


Figure 11. (a) Schematic of the chemical crosstalk between the cathode and anode within the full cell. (b) Configuration of the crosstalk effect between the C_2H_4 gas generated from SEI decomposition and cathode.

The gas amount is critical in determining the battery performance and safety state. The increase in gas generation in lithium batteries can reduce cycling stability. The crosstalk of gas generation between the positive and negative electrodes may trigger thermal runaway in the battery. Dong et al. adopted a polymer electrolyte, which significantly reduced gas generation at the electrolyte-electrode interface, thereby mitigating interfacial exothermic reactions and subsequent gas crosstalk [34]. This approach markedly enhanced battery safety. He et al. applied a carbon coating on the anode surface, which suppressed reactions at the electrolyte-anode interface and substantially minimized gas generation on the anode side [65]. Hu et al. implemented a coating modification on NCM622, effectively reducing oxygen release from the cathode [66]. This modification alleviated oxygen-induced crosstalk to the anode, improving both cycling stability and thermal stability of the battery. As gas generation within lithium-ion batteries gradually increases, the battery first undergoes

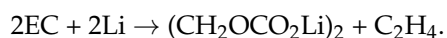
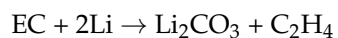
physical structural changes induced by gas accumulation. Continuous gas production in the confined space elevates internal pressure, causing cell expansion [44]. Pouch cells, due to their flexible packaging, are particularly prone to localized deformation, leading to electrode wrinkling and compression of separator pores.

4. Electrolytes

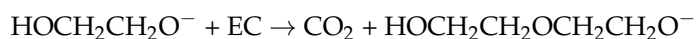
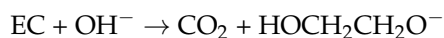
Electrolytes are critical components of lithium-ion batteries, often referred to as the “blood” of the battery. They facilitate ion transport between the electrodes and suppress parasitic reactions at the electrode/electrolyte interface by forming protective layers [67]. Electrolytes also significantly impact battery safety. This section reviews gas evolution behaviors in liquid- and solid-state electrolytes [68].

4.1. Liquid Electrolytes

Liquid electrolytes in rechargeable lithium-ion batteries typically consist of linear and cyclic alkyl carbonate blends, such as EC, propylene carbonate (PC), dimethyl carbonate (DMC), diethyl carbonate (DEC), and EMC, with LiPF₆ as the lithium salt. Gas evolution primarily stems from electrolyte decomposition and reactions with active materials. During initial cycling, electrolyte decomposition during SEI formation releases gases. Under abusive conditions (overcharge, high temperature), electrolytes react extensively with electrode materials, generating large volumes of gas and heat, leading to thermal runaway or even explosion [69]. EC is the most common electrolyte solvent. During initial cycling, EC reacts with active lithium at the anode to form the SEI, producing C₂H₄ gas via [70]:



EC decomposition occurs via two pathways: (1) direct electrochemical decomposition at the cathode generates CO, intermediates, and protonated solvents, which are reduced to H₂ at the anode. (2) Oxidative decomposition with reactive oxygen atoms from the cathode produces CO and H₂O. Oxidative decomposition dominates under high voltage, while elevated temperatures (e.g., 60 °C) balance both pathways [71]. Trace water generates OH⁻, triggering EC autocatalytic reactions to produce CO₂ [45]:



At 85 °C, 52% of CO₂ and 60% of CO originate from EC decomposition. EC reduction dominates at the anode surface, regardless of co-solvents (DMC or DEC) [70]. PC exhibits excellent low-temperature performance, high ionic conductivity, and low toxicity [72]. Its reaction pathway resembles EC. As shown in Figure 12a,b, during initial cycling, PC reacts with lithium to form lithium propylene dicarbonate (LPDC) and C₃H₆ gas. OH⁻-induced ring opening produces CO₂. Unlike EC-derived SEI components, LPDC exhibits higher solubility, leading to SEI dissolution and graphite exfoliation in PC-rich electrolytes (>30% PC) [70]. Li₂CO₃ forms the final SEI layer. Poor wettability with electrodes and separators limits PC's commercial adoption [73,74]. DMC, DEC, and EMC decompose to generate CH₄ and CO via (Figure 13) [75,76]:



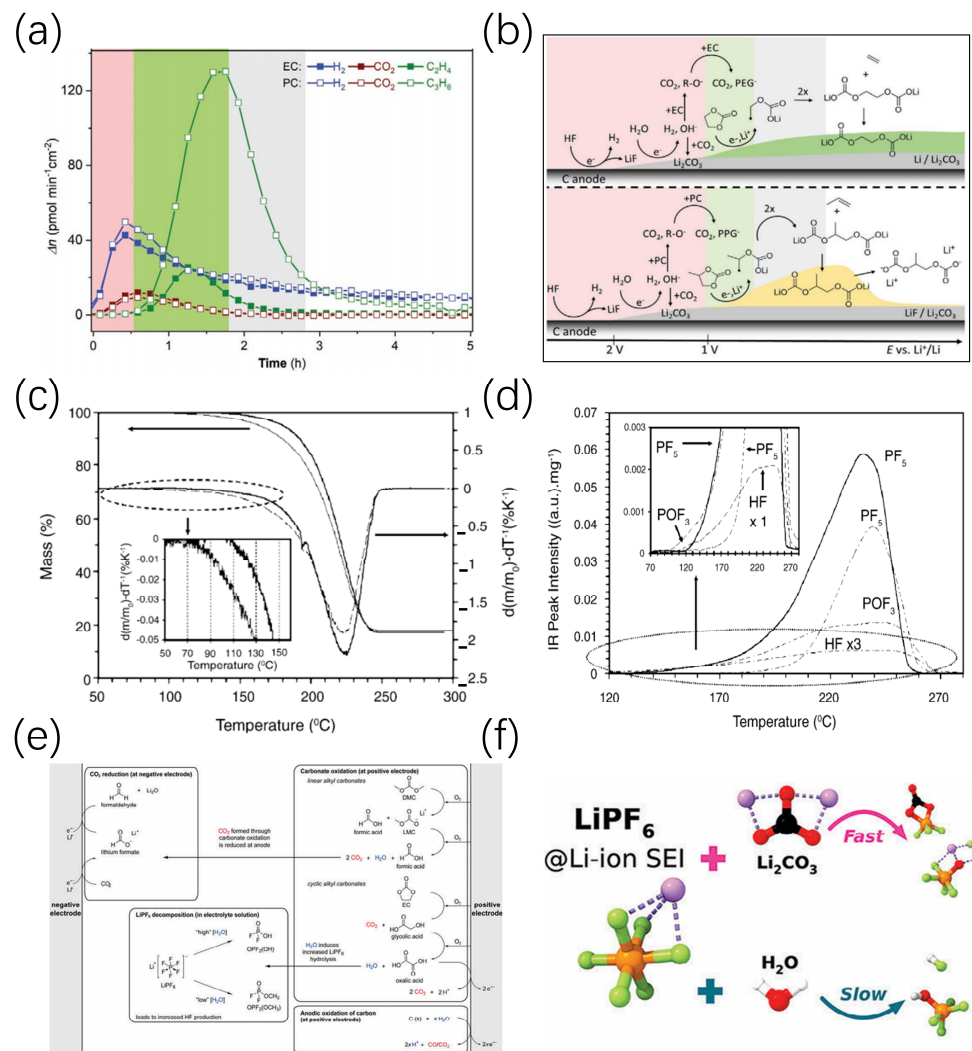
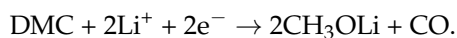
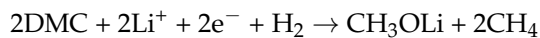
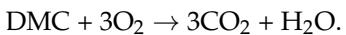


Figure 12. (a) Associated gas evolution rates in EC:DEC (1:1 vol%) and in PC. (b) Schematic of the SEI formation process in EC-based electrolyte and PC-based electrolyte [77]. (c) Mass loss (left) and rate of mass loss (right) during thermal decomposition of LiPF_6 containing <10 ppm H_2O (solid line) and with 300 ppm water vapor (dashed line). (d) Evolution of gaseous products as a function of temperature during thermal decomposition of LiPF_6 containing less than 10 ppm water (solid line) and with 300 ppm water vapor (dashed line) [78]. (e) Overview of electrolyte decomposition reactions that occur at high SOC/voltages initiated at the positive electrode [79]. (f) Comparison of two pathways for LiPF_6 decomposition [79].

Overcharge conditions accelerate gas evolution. DMC reacts with lattice oxygen to produce CO_2 [80]:



DEC and EMC follow similar decomposition mechanisms [75].

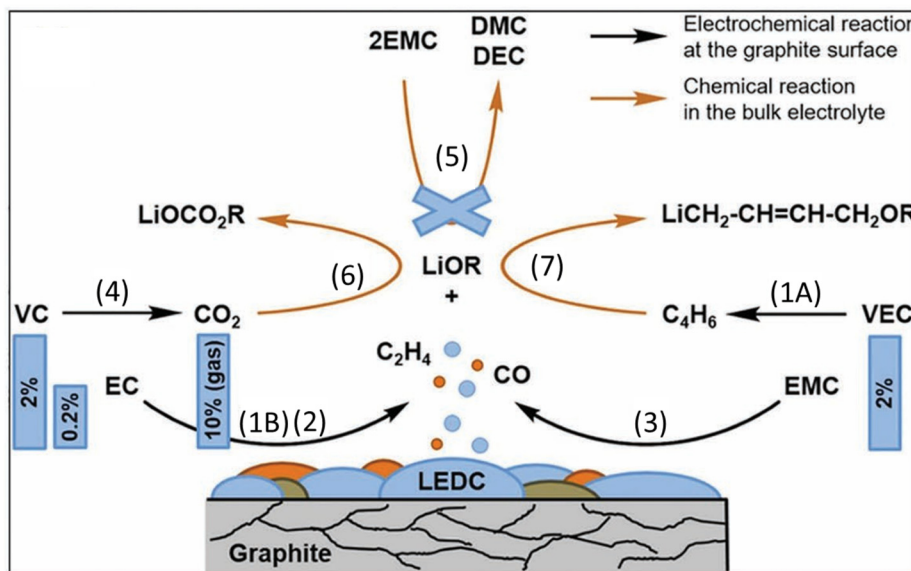


Figure 13. Schematic diagram of interface formation and gas production of electrolyte on anode surface [81]. The numbers (1), (2), etc. in the figure indicate the sequential numbering of electrolyte reaction pathways.

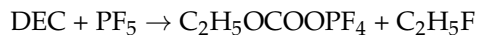
LiPF_6 is the most widely used lithium salt due to its high conductivity, excellent electrochemical stability, and low cost. It is extensively employed in commercial lithium-ion batteries. However, LiPF_6 has several drawbacks, including poor thermal stability, susceptibility to decomposition at high temperatures, and extreme sensitivity to moisture. As shown in Figure 12c,d, pure LiPF_6 decomposes at 107°C in dry environments, but remains stable at 90°C . In the presence of trace water (300 ppm), decomposition occurs at 87°C [78]. No thermally induced reactions have been observed between LiPF_6 and common solvents such as EC, DMC, or EMC. LiPF_6 readily decomposes to produce LiF and PF_5 gas, as described by the reaction (Figure 12e):



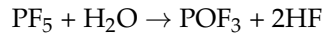
In the presence of water, LiPF_6 reacts to generate POF_3 and HF gases [82]:



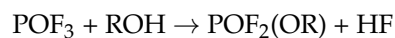
Thermal abuse tests on batteries detect the presence of HF and POF_3 in the evolved gases (Figure 12f) [83]. As shown in Figure 14, both PF_5 and POF_3 can further decompose solvent molecules, leading to significant gas generation [82]. For example, PF_5 reacts with DEC to produce C_2H_4 , HF, and $\text{C}_2\text{H}_5\text{F}$:



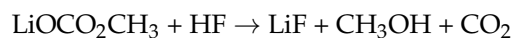
PF_5 can also react with water to regenerate HF and POF_3 [83]:



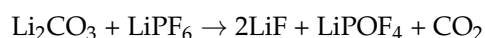
At excessively high voltages, carbonate solvents oxidize to form ROH species, which react with PF_5 to produce HF and POF_3 :



HF gas reacts with organic components in the SEI, releasing CO₂ and damaging the SEI:



HF also promotes the leaching of transition metal ions (e.g., Mn) from cathode materials, further degrading the SEI and exposing the anode to electrolyte reactions, resulting in additional gas evolution. HF is highly toxic, posing severe health risks upon exposure. Combustion tests on seven commercial battery types revealed significant HF emissions [84]. LiPF₆ can react with Li₂CO₃ to produce CO₂:



While LiPF₆ performs well under normal operating conditions, the presence of trace water or abusive conditions (overcharge, overheating) triggers complex reactions, generating large volumes of gas and severely compromising battery capacity and safety. Therefore, developing low-cost, high-conductivity, and non-toxic alternatives to LiPF₆ is a critical direction for improving lithium-ion battery safety.

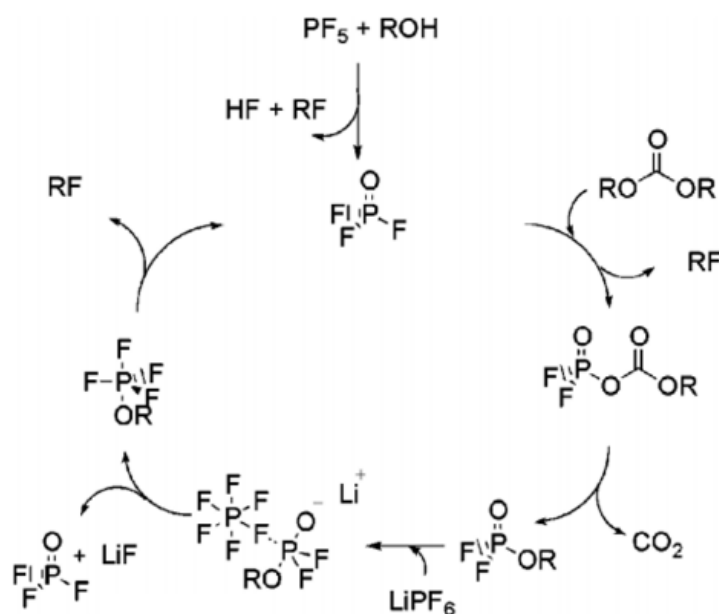


Figure 14. Autocatalytic reaction mechanism for the decomposition of lithium-ion battery electrolytes composed of LiPF₆ and carbonate solvents [85].

Electrolyte decomposition is a central driver of gas generation and thermal runaway in lithium-ion batteries. Liquid electrolytes, primarily composed of LiPF₆ and carbonate solvents, undergo redox reactions and thermal degradation under abusive conditions. At elevated temperatures (>80 °C), the SEI on the anode decomposes, releasing heat and flammable gases (e.g., H₂, C₂H₄). Simultaneously, LiPF₆ hydrolysis generates HF and POF₃, which corrode electrodes and catalyze further electrolyte decomposition. Above 150 °C, solvents like EC oxidize exothermically, producing CO₂ and hydrocarbons (CH₄, C₂H₄), while residual water triggers autocatalytic reactions, accelerating gas evolution. These gases accumulate, increasing internal pressure and inducing mechanical stress, which

disrupts ion transport and elevates local temperatures. Combustible gases (H_2 , CH_4) mix with oxygen from cathode decomposition, forming explosive mixtures that ignite upon reaching critical concentrations. This creates a self-sustaining “gas–heat” cycle: heat accelerates electrolyte breakdown, releasing more gas, while gas expansion exacerbates thermal gradients.

4.2. Solid-State Electrolytes

4.2.1. Sulfide Electrolytes

Sulfide-based solid-state electrolytes (SSEs) hold significant promise due to their excellent room temperature ductility and high ionic conductivity, with some even rivaling liquid electrolytes. However, sulfide electrolytes suffer from critical drawbacks, including poor air stability and the tendency to generate toxic H_2S gas [86]. Researchers investigated $\text{Li}_2\text{S}-\text{P}_2\text{S}_5$ sulfide-based solid-state electrolytes and discovered that exposure to atmospheric moisture (H_2O) triggers the generation of H_2S gas. A detailed mechanism for H_2S formation was proposed [87].

$\beta\text{-Li}_3\text{PS}_4$, a common sulfide SSE, exhibits high ionic conductivity (0.5 mS/cm). Torsten Brezesinski’s team conducted extensive studies on $\beta\text{-Li}_3\text{PS}_4$ [6,88,89]. During normal cycling at 45 °C, no H_2S evolution was detected in cells with Li_2TiO_3 or indium anodes paired with NCM cathodes. However, SO_2 release was observed in cells with indium anodes, closely linked to O_2 evolution. The decomposition of surface carbonates generates highly reactive oxygen species, which react with $\beta\text{-Li}_3\text{PS}_4$ to form SO_2 . In contrast, $\text{Li}_6\text{PS}_5\text{Cl}$ SSEs show no H_2S or SO_2 generation. First-principles calculations indicate that all sulfide electrolytes produce sulfur (S) under high voltages [90]. SO_2 formation likely results from interactions between sulfur and reactive oxygen species. Addressing gas evolution in sulfide SSEs is crucial for advancing their development and application.

The H_2S generation rate was derived by computing the first-order derivative of cumulative H_2S production over time (Figure 15a,b). For Li_3PS_4 (LPS), the rate peaks at approximately 22 min of exposure before declining, whereas lithium silicon sulfide (LSS) and lithium aluminum sulfide (LSAS) exhibit maximum rates within the first minute, followed by a steady decrease. Notably, lithium silicon phosphorus sulfur chloride (LSPSC) displays fluctuating rates with three distinct peaks: an initial peak at ~1 min and subsequent peaks at 16.8 and 164 min. These fluctuations likely arise from multistep hydrolysis reactions inherent to LSPSC. This demonstrates that incorporating transition metal oxides effectively suppresses H_2S release from sulfide electrolytes during exposure [91].

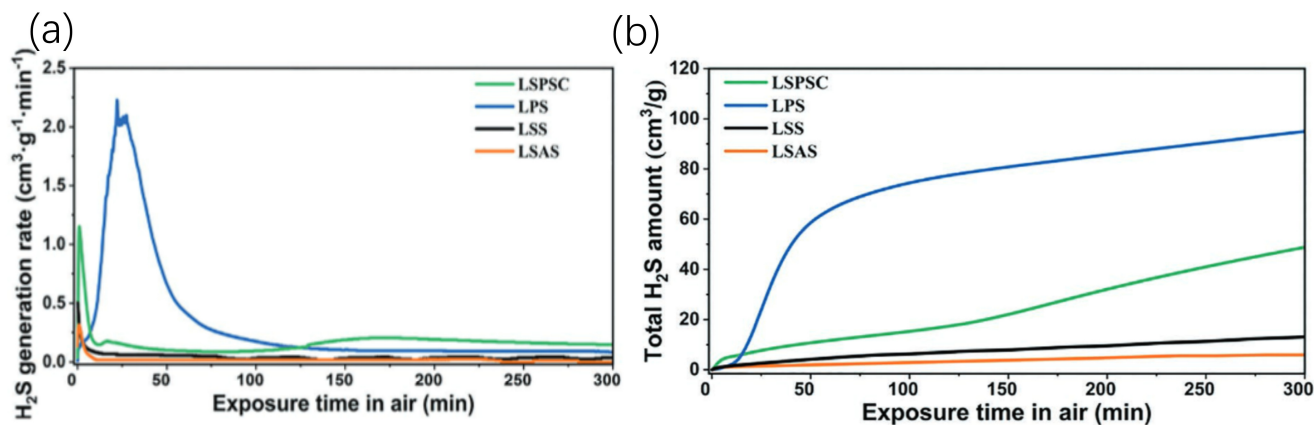


Figure 15. (a) Relationship between H_2S release rate and exposure time for four sulfide electrolytes: LSPSC, LPS, LSS, and LSAS [92]. (b) Diagram of the relationship between H_2S production and exposure time [92].

4.2.2. Oxide Electrolytes

Compared to sulfide electrolytes, oxide-based SSEs exhibit a wider electrochemical window and superior high-voltage stability. Oxide SSEs such as lithium lanthanum titanium oxide (LLTO), lithium lanthanum zirconium oxide (LLZO), lithium aluminum titanium phosphate (LATP), lithium aluminum germanium phosphate (LAGP), and lithium super ionic conductor (LISICON) release O₂ at extremely high voltages (above 5 V) [93]. Yasmine Benabed et al. investigated LAGP and LATP oxide SSEs, finding that LAGP operates stably within 1.85–4.9 V, while LATP remains stable within 2.65–4.6 V. Beyond these voltage ranges, the electrolytes decompose, generating various oxides and releasing O₂ gas at high voltages [94]. Overall, oxide SSEs demonstrate stable performance within their electrochemical stability windows, and gas evolution is not a significant issue under normal operating conditions [95].

4.2.3. PEO-Based Polymer Electrolytes

Poly (ethylene oxide) (PEO)-based polymer electrolytes demonstrate favorable attributes such as electrode adhesion, flexibility, and low cost. However, their primary limitation is low ionic conductivity at room temperature. Wu et al. developed a simple and cost-effective PEO/LiTFSI polymer electrolyte, enabling the operation of all-solid-state LiFePO₄ (LFP)/PPL/Li cells at 30 °C, demonstrating potential for practical applications [96]. PEO-based polymer electrolytes exhibit good thermal stability. For instance, PEO-LiCF₃SO₃ and PEO-LiN(CF₃SO₂)₂ remain stable up to 300 °C, although their decomposition temperature decreases when in contact with cathode materials, particularly under charged states at 4 V. Nevertheless, PEO-based cells operate stably within the 60–100 °C range without significant gas evolution.

PEO/LiTFSI maintains stability against lithium anodes up to 4.5 V but undergoes decomposition at approximately 3.8 V when in contact with carbon composite electrodes, as the high-surface-area carbon catalyzes polymer decomposition [97,98]. Gas evolution in PEO-based electrolytes begins at 4.5 V. As shown in Figure 16, in LiCoO₂ | PEO-LiTFSI | Li cells, noticeable H₂ generation occurs at 4.2 V, while a variety of gases, including H₂, CH₄, H₂O, C₂H₂, C₂H₄, CO, C₂H₆, HCHO, O₂, CH₃OH, CO₂, CH₃CHO, CH₃CH₂OH, and HCOOH, are released at 4.5 V. Studies suggest that the LiCoO₂ surface catalyzes PEO decomposition and HTFSI formation, with HTFSI reacting with metallic lithium to produce H₂ (Figure 16e). Coating PEO with LATP enhances its stability, suppressing gas evolution even at 4.6 V [99]. While PEO-based polymer electrolytes hold significant potential for future development, research on their gas evolution behavior remains limited. Further efforts are necessary to explore and address these challenges to advance their practical application.

4.2.4. Gassing Behavior and Thermal Runway in SSB

The thermal runaway mechanism in solid-state electrolytes fundamentally involves a tripartite coupling of gas generation, heat accumulation, and structural failure. Thermal runaway is typically triggered by localized temperature anomalies, such as internal short circuits or external thermal abuse, where chemical instability at the electrolyte-electrode interface induces side reactions that release gases including H₂S, CO₂, H₂, and hydrocarbons. These gases establish a positive feedback loop through physical expansion and chemical exothermicity, driving the escalation of thermal runaway.

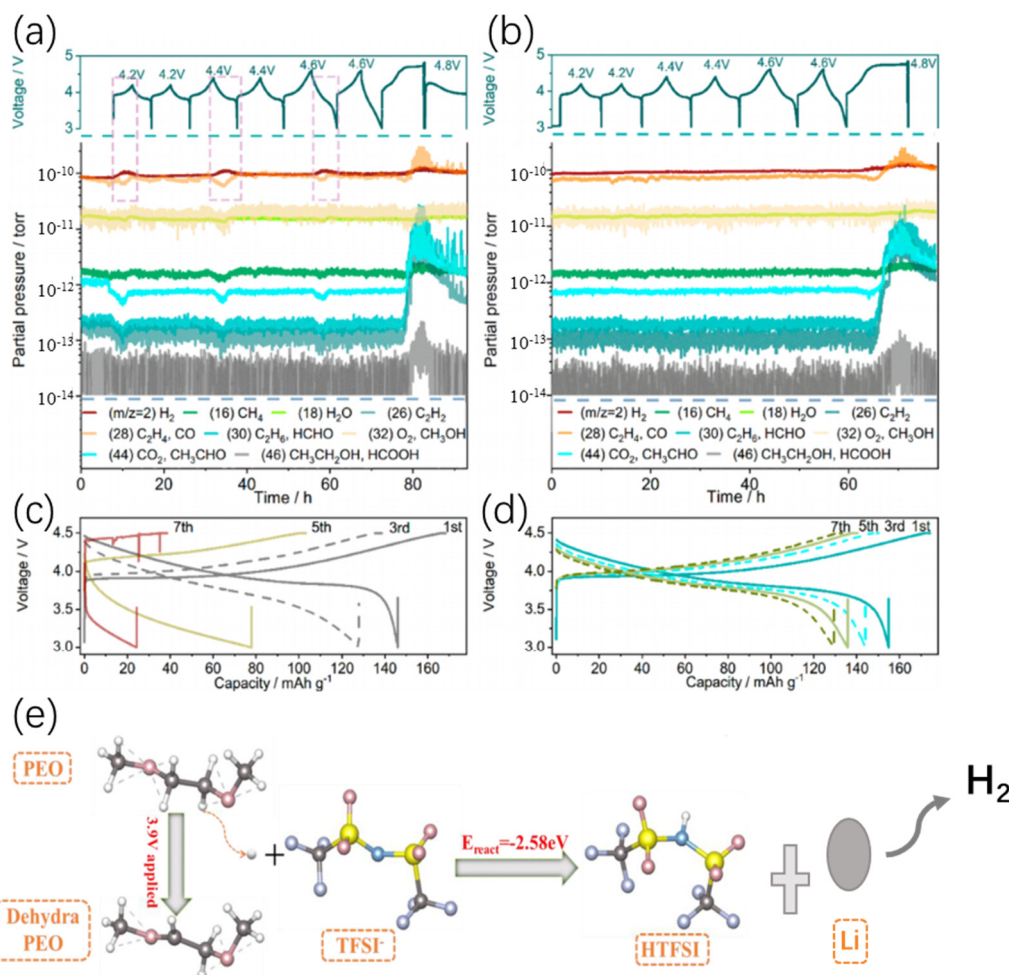


Figure 16. Voltage profile and corresponding mass signals of (a) the $\text{LiCoO}_2 \mid \text{PEO-LiTFSI} \mid \text{Li}$ cell and (b) the $\text{LATP-LiCoO}_2 \mid \text{PEO-LiTFSI} \mid \text{Li}$ cell [100]. (c) $\text{LiCoO}_2 \mid \text{PEO-LiTFSI} \mid \text{Li}$ cell and (d) $\text{LATP-LiCoO}_2 \mid \text{PEO-LiTFSI} \mid \text{Li}$ cell charge–discharge curves. (e) PEO generates HTFSI and reacts with lithium metal through a pathway producing H_2 [99].

During the initial stage of thermal runaway, distinct gas generation pathways emerge across different electrolyte systems. Sulfide electrolytes react with residual liquid electrolyte solvents to produce corrosive H_2S and SO_2 , which further react with lithium metal to form sulfides, releasing heat and causing a sharp rise in interfacial impedance. Oxide electrolytes undergo decomposition of surface Li_2CO_3 impurities, releasing CO_2 that reacts exothermically with lithium metal to form Li_2O and create localized hotspots, accelerating lattice oxygen loss. Polymer electrolytes experience backbone pyrolysis, generating low-molecular-weight hydrocarbons (e.g., CH_4 , C_2H_4), while acidic byproducts from lithium salt hydrolysis react with lithium metal to release H_2 , forming flammable gas mixtures. Although gas accumulation at this stage does not directly ignite combustion, it significantly weakens mechanical stability, leading to electrode-electrolyte contact failure. As temperatures escalate to intermediate and high levels, gas generation and heat release enter a self-reinforcing cycle. In sulfide systems, H_2S reacts with electrolyte decomposition products (e.g., PF_5) to form sulfur-containing polymers or sulfur vapor, blocking ion transport channels and catalyzing chain decomposition of the electrolyte with substantial heat release. In oxide systems, continuous CO_2 generation combined with heat from lithium metal reactions promotes oxygen vacancy aggregation and subsequent O_2 release, which reacts violently with residual liquid components to release intense heat. Polymer systems exhibit explosive atmospheres from the mixing of H_2 and cathode-released O_2 , leading to localized

ignition and instantaneous heat release. At this stage, gas-driven physical expansion and chemical exothermicity exacerbate structural damage, pushing thermal runaway toward irreversibility. Under extreme high temperatures, thermal runaway enters its terminal phase. Sulfide electrolytes fully decompose into sulfur vapor and metal sulfides, reacting violently with lithium metal and triggering gas-phase combustion. Oxide electrolytes release O₂ that reacts with carbon-based residues to generate CO/CO₂ with intense heat release (Figure 17). Hydrocarbon gases in polymer systems undergo thermal cracking into soot and hydrogen, intensifying combustion severity. Internal pressure surges exceeding structural limits cause casing rupture, releasing high-temperature flammable gases that ignite upon external oxygen exposure, resulting in secondary combustion or explosions.

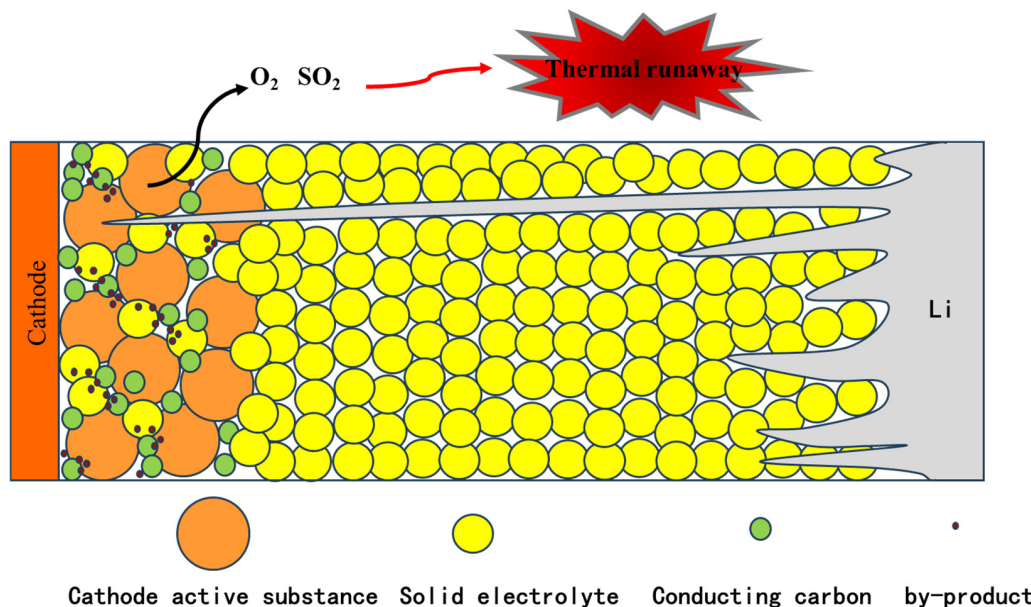


Figure 17. Mechanisms of thermal runaway in batteries, including interface/Li interactions, O₂ release, and its reaction with Li metal.

Research highlights that the core driver of thermal runaway lies in the synergistic interplay of “gas–heat–structural failure”: gas generation elevates system entropy through chemical exothermicity and pressure buildup; heat accelerates material decomposition and interfacial reactions, releasing additional gas; and structural failures (e.g., separator melting, electrode delamination) disrupt heat dissipation, amplifying localized temperature spikes. To suppress this vicious cycle, strategies must target both intrinsic material stability (e.g., grain boundary doping for sulfides, surface passivation for oxides) and interfacial optimization (e.g., composite electrolytes, functional coatings). Integration of in situ monitoring and multi-physics modeling will further advance the design of inherently safe solid-state batteries with high energy density.

Gas generation mechanisms in liquid and solid electrolytes differ significantly in their impacts on cycling, failure, and thermal runaway. In liquid electrolytes, gas primarily arises from solvent oxidation/reduction (e.g., carbonate decomposition into CO₂, H₂, C₂H₄) and lithium salt (LiPF₆) hydrolysis. Gas accumulation depletes electrolytes, disrupts SEI stability, and increases impedance. High-voltage systems (>4.3 V) exhibit 2–3 times higher solvent oxidation gas yields, accelerating capacity fade. Solid electrolytes (e.g., oxides, sulfides, polymers) generate gases mainly through interfacial side reactions: oxide electrolytes (e.g., LLZO) release CO₂ via Li₂CO₃ impurity decomposition at lithium metal interfaces; sulfide electrolytes (e.g., LPS) produce SO₂ or H₂S via sulfur oxidation at high-potential cathode interfaces; polymer electrolytes (e.g., PEO-based) release hydrocarbons (e.g., CH₄)

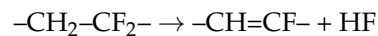
under high voltage. Lithium dendrite growth may also induce local electrolyte decomposition or solid electrolyte reduction (e.g., Li_3P from LPS decomposition), forming pores and degrading ion transport. In failure mechanisms, liquid electrolyte gases block active sites and catalyze cross-reactions (e.g., H_2 migration to the cathode for oxidation). In solid electrolytes, gases accumulate at interfaces, forming “gas gaps” that increase interfacial impedance (>50%). Sulfide-derived H_2S poisons cathodes, while polymer electrolyte gases induce layer delamination.

5. Other Components

In addition to electrodes and electrolytes, additives such as binders, conductive carbons, and residual Li_2CO_3 on cathode surfaces can also contribute to gas generation, despite their minor proportions in batteries. Investigating their gas evolution behaviors is essential.

5.1. PVDF Binder

Organic binders are commonly used to adhere active materials to current collectors. PVDF is a preferred choice in commercial lithium-ion batteries due to its excellent mechanical, chemical, and electrochemical properties [101,102]. Although chemically stable, PVDF can generate gases during battery operation. In alkaline environments, PVDF undergoes dehydrofluorination to produce HF gas:



As previously mentioned, HF generation induces transition metal dissolution, severely degrading battery performance by accelerating gas evolution and capacity fade—a critical drawback of fluorine-containing PVDF [64].

Yang Jin et al. observed H_2 generation during overcharge conditions when PVDF reacts with lithium dendrites deposited on graphite anodes (Figure 18) [103]. Other binders, such as styrene–butadiene rubber (SBR) and carboxymethyl cellulose (CMC), exhibit similar issues, with H_2 evolution occurring even earlier [103]. Despite the severe consequences of PVDF-induced gas generation, no superior alternatives have yet been identified. Minimizing HF production remains a key priority when using PVDF binders.

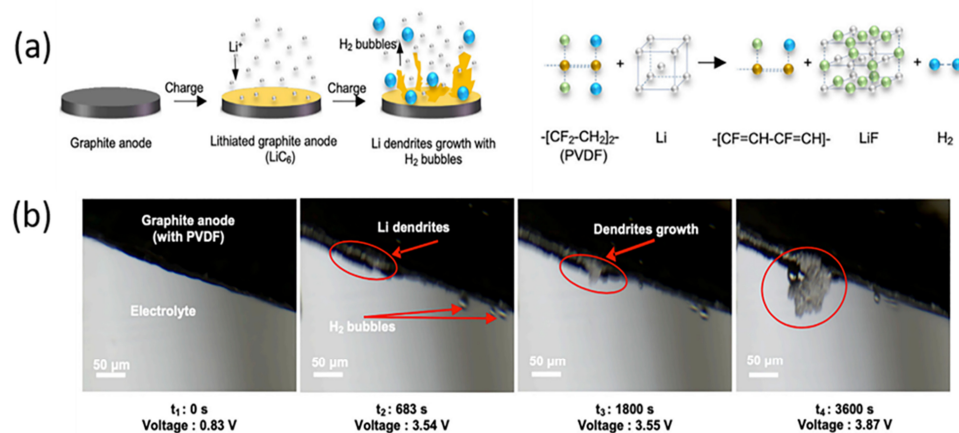


Figure 18. (a) Schematic of Li dendrite growth detection by H_2 gas capture. (b) In situ experiments of Li dendrite detection and H_2 gas capture with presence of polymer binder of graphite anode surface during the charging process [103].

5.2. Conductive Carbon

In lithium battery electrode materials, the incorporation of inactive conductive carbon as an additive is a prevalent strategy to enhance electronic conductivity while maintaining

cost-effectiveness. The physicochemical properties of conductive carbon play a critical role in its gas evolution behavior. High-specific-surface-area carbon materials, such as Super P, increase the effective contact area of the SEI, leading to elevated electrolyte consumption and intensified gas generation during initial cycling. The incorporation of such conductive agents reduces the onset temperature of thermal runaway by approximately 20 °C, compromises the chemical stability of the system, and promotes gas generation through accelerated decomposition reactions [104]. Moreover, these materials induce significant gas-related side reactions under high-voltage operating conditions. Further studies reveal that non-active conductive carbon exhibits electrochemical activity under high-voltage conditions. High-surface-area carbon provides abundant reactive sites for electrolyte decomposition, narrowing the electrochemical stability window. Even low-surface-area carbon materials undergo electrolyte decomposition and functional group oxidation on their surfaces during high-voltage operation, generating substantial gas [105]. Notably, a polymer film resembling the interface formed by electrolyte oxidation on conductive carbon surfaces can mitigate further decomposition and gas generation [106].

As shown in Figure 19a–c, Michael Metzger demonstrated that conductive carbon undergoes anodic oxidation at high voltages, producing CO₂ and CO gases, particularly under high-temperature and moisture-rich environments [107]. Similarly, isotopic ¹³C labeling experiments confirmed that carbon coatings on lithium LFP cathodes release ¹³CO₂ and ¹³CO upon oxidation at high voltages, with moisture accelerating gas evolution (Figure 19b,c) [108]. In cathode materials, conductive carbon not only lowers the onset voltage of gas evolution, but also catalyzes the oxidative decomposition of the electrolyte [106]. For instance, during storage at 60 °C, gas generation predominantly occurs at conductive carbon surfaces rather than on cathode active materials (e.g., LNMO), and the specific surface area of the carbon correlates positively with gas production. At voltages around 4.7 V, anions (e.g., PF₆⁻) intercalate into the conductive carbon structure (e.g., Super P), accompanied by electrolyte decomposition and gas evolution [109].

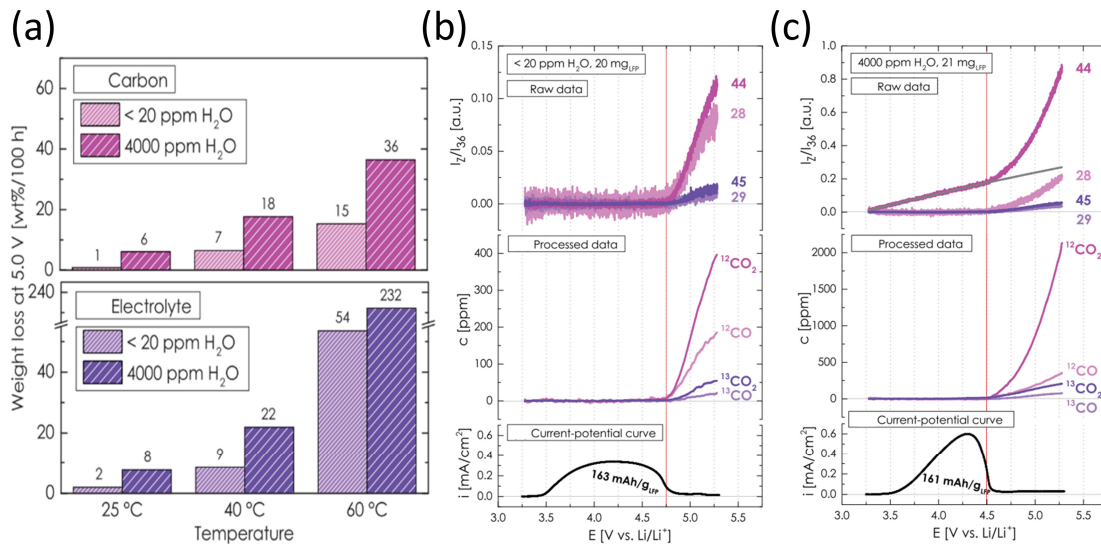
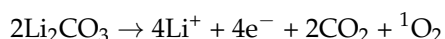


Figure 19. (a) Accumulated weight loss of conductive of carbon and electrolyte over 100 h at a potential of 5.0 V [107]. (b) H₂O < ppm and (c) 4000 ppm H₂O evolution of CO₂ and CO for a LFP-¹³C working electrode [108].

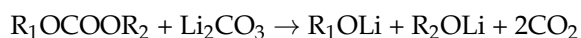
Although conductive carbon additives are essential for electrode conductivity, their induced gas-related side reactions significantly reduce battery stability, exacerbate safety risks, and may limit the practical application of high-voltage cathode materials.

5.3. Li_2CO_3

Residual Li_2CO_3 often remains on the surface of cathode materials. As shown in Figure 20, Toru Hatsukade et al. employed ^{13}C isotopic labeling to trace Li_2CO_3 on NCM surfaces, revealing significant decomposition of Li_2CO_3 at high potentials during the first cycle, generating CO_2 [110]. Using ^{18}O isotopic labeling, it was demonstrated that the generation of CO_2 and CO during the initial cycle is almost entirely attributed to the decomposition of Li_2CO_3 , with negligible contribution from electrolyte decomposition at the cathode [111]. As shown in Figure 20b, by using 9,10-dimethylantracene (DMA), it was discovered that Li_2CO_3 decomposes at 3.8 V to generate highly reactive $^1\text{O}_2$, which is not released as molecular oxygen (O_2). The decomposition reaction is described as [112]:



Li_2CO_3 on cathode surfaces reacts with dialkyl carbonate solvents in the presence of catalysts to generate CO_2 :



Additionally, Li_2CO_3 reacts with LiPF_6 to produce CO_2 :



Washing NCA cathodes to remove surface Li_2CO_3 significantly reduces gas evolution. Therefore, thorough cleaning of cathodes during manufacturing is critical to minimize residual Li_2CO_3 and mitigate gas generation.

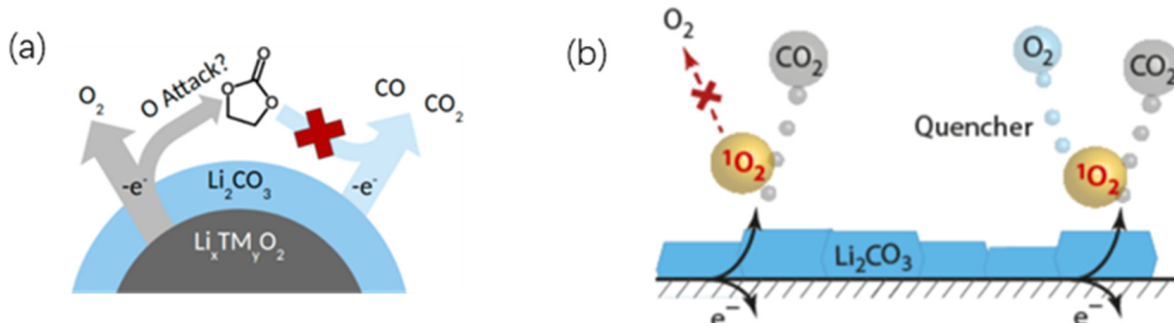


Figure 20. (a) Schematic diagram of CO_2 and CO gas generation during the initial charging and discharging process [111]. (b) Electrochemical oxidation of lithium carbonate generates singlet oxygen [112].

Gas generation from non-active components (e.g., binders, conductive agents) also impacts battery performance. PVDF binders release HF via defluorination under high voltage/temperature, corroding cathodes and degrading conductive networks. HF accelerates electrolyte decomposition, generating CO_2 and PF_5 , while residual fluorinated carbons increase interfacial polarization. Conductive carbon surfaces catalyze electrolyte redox reactions, clogging pores and impeding ion diffusion. Carbon agglomeration worsens cycling stability, and carbon–electrolyte reactions form porous SEI layers, increasing impedance. Residual Li_2CO_3 on electrodes decomposes at high voltage/temperature, releasing CO_2 and O_2 , depleting electrolytes and thickening CEI. CO_2 accumulation causes cell swelling and electrode delamination, while O_2 migrates to the anode, reacting with lithium to form Li_2O and active lithium loss.

During thermal runaway, PVDF-derived fluorinated gases mix with cathode-released O₂ to form explosive atmospheres, releasing intense heat. Conductive carbon accelerates electrolyte decomposition (e.g., C₂H₄, CO) and oxidizes exothermically, elevating temperature rise rates. Li₂CO₃ decomposition releases O₂, which reacts with combustible gases (e.g., C₂H₄) to transition thermal runaway from slow heat generation to combustion. PVDF–lithium reactions, Li₂CO₃-induced lithium loss, and carbon-driven local hotspots collectively form a multi-path gas–heat coupling mechanism, complicating failure and thermal runaway.

The cell failure originates from the chemical and structural degradation of electrode materials and electrolytes, progressively spreading to the entire battery system through deteriorating interfacial reactions. Under high voltage or elevated temperatures, cathode materials undergo lattice oxygen release and transition metal dissolution. The dissolved metal ions migrate to the anode and become embedded in the SEI [113], forming catalytic active sites that accelerate electrolyte reduction and decomposition, releasing gases such as CO₂ and hydrocarbons. Concurrently, volume expansion in silicon-based or high-capacity graphite anodes during lithium intercalation causes SEI layer rupture. The newly exposed active surfaces continuously trigger electrolyte decomposition, further consuming active lithium and releasing gases [114].

When gas accumulation within a single cell reaches a critical level, the internal pressure rises significantly, causing cell casing deformation and imposing additional mechanical stress on adjacent cells within the module. Furthermore, when a single cell undergoes thermal runaway due to the aforementioned interfacial reactions [115], high-temperature electrolytes and ejected gases rapidly heat neighboring cells, causing separator shrinkage and increasing internal short-circuit risks [116]. Gas diffusion within the confined module space creates flammable mixtures, where even minor sparks can ignite the entire module. Simultaneously, coordinated cell expansion distorts module structure, deforming mounting brackets and loosening busbar connections [117]. Elevated contact resistance induces localized overheating, creating new thermal runaway triggers.

6. Conclusions and Perspectives

Gas generation during battery operation—whether through normal aging or abusive conditions—triggers cascading failures ranging from performance degradation (capacity fade, impedance rise) to catastrophic safety risks (thermal runaway). This review establishes critical structure–property relationships between material degradation pathways and their gas evolution mechanisms across battery components:

1. Cathode materials: future strategies focus on stabilizing oxygen lattices and suppressing gas-inducing side reactions. Key approaches include dynamic oxygen reservoir engineering using redox mediators to trap released oxygen as solid intermediates, high-entropy cation/anion co-doping to disrupt oxygen migration pathways, and bio-inspired self-healing coatings that decompose reactive oxygen species. Advanced atomic-layer techniques will enable gradient oxygen coordination environments, dynamically adjusting bonding strength during cycling to prevent collective oxygen escape.
2. Anode materials: innovations target lithium deposition control and volume expansion management. For lithium metal, electrocatalytic artificial SEI layers with embedded nanoparticles can homogenize Li⁺ flux while converting gaseous byproducts into solids. Silicon anodes require stress-adaptive 3D porous frameworks with gas-absorbing ionic liquid electrolytes to mitigate SEI cracking. Graphite modifications include anisotropic edge engineering to prevent low-temperature solvent

co-intercalation and molecular sieve-integrated separators to trap gases before bubble formation.

3. Cross-material synergy: emerging systems leverage electrode interactions for gas mitigation, such as coupling oxygen-scavenging cathode coatings with H₂-absorbing anode additives to neutralize gaseous intermediates. Operando gas recycling could electrochemically reconvert CO₂/O₂ into SEI/CEI components, transforming gas into a self-healing resource. Integrated designs must combine atomic-scale simulations, multifunctional architectures, and closed-loop gas management to break the gas degradation cycle while advancing energy density.
4. Electrolytes: beyond conventional LiPF₆ optimization, two strategies are proposed: (i) high-entropy multi-salt systems to balance ion transport and interfacial stability, and (ii) solvation structure engineering to form gas-suppressing dense SEI/CEI layers. Solid-state electrolytes emerge as a transformative solution to minimize gas evolution.
5. Auxiliary components: fluorine-free binders and surface-modified conductive agents (e.g., S-doped carbons) are prioritized to eliminate HF generation and redirect electrolyte decomposition toward solid-phase products.

These advanced strategies transcend conventional component-specific optimizations, offering integrated solutions to break the gas degradation feedback loop while pushing energy density boundaries. Their implementation will require coordinated advances in atomic-scale simulation-guided design, additive manufacturing of multifunctional architectures, and closed-loop gas management systems.

Funding: This work is financially supported by the National Natural Science Foundation of China (52203283).

Data Availability Statement: No new data were created or analyzed in this study. Data sharing is not applicable to this article.

Conflicts of Interest: All authors declare no conflicts of interest.

References

1. Yan, W.; Ma, L.; Xu, J.; Guo, Y.; Hu, H.; Zhi, C.; Ho, D. Battery-Sensor Hybrid: A New Gas Sensing Paradigm with Complete Energy Self-Sufficiency. *Accts Appl. Mater. Interfaces* **2021**, *13*, 46507–46517. [[CrossRef](#)] [[PubMed](#)]
2. Kong, W.; Zhang, J.; Wong, D.; Yang, W.; Yang, J.; Schulze, C.; Liu, X. Tailoring Co3d and O2p band centers to inhibit oxygen escape for stable 4.6V LiCoO₂ cathodes. *Angew. Chem. Int. Ed. Engl.* **2021**, *133*, 27308–27318. [[CrossRef](#)]
3. Schiele, A.; Breitung, B.; Hatsukade, T.; Berkes, B.B.; Hartmann, P.; Janek, J.; Brezesinski, T. The Critical Role of Fluoroethylene Carbonate in the Gassing of Silicon Anodes for Lithium-Ion Batteries. *ACS Energy Lett.* **2017**, *2*, 2228–2233. [[CrossRef](#)]
4. Ge, B.; Hu, L.; Yu, X.; Wang, L.; Fernandez, C.; Yang, N.; Liang, Q.; Yang, Q.H. Engineering Triple-Phase Interfaces around the Anode toward Practical Alkali Metal–Air Batteries. *Adv. Mater.* **2024**, *36*, e2400937. [[CrossRef](#)]
5. Chen, B.; Jiang, H.; Chen, X.; Li, H. Robust state-of-charge estimation for lithium-ion batteries based on an improved gas-liquid dynamics model. *Energy* **2022**, *238*, 122008. [[CrossRef](#)]
6. Jozwiuk, A.; Berkes, B.B.; Weiss, T.; Sommer, H.; Janek, J.; Brezesinski, T. The critical role of lithium nitrate in the gas evolution of lithium-sulfur batteries. *Energy Environ. Sci.* **2016**, *9*, 2603–2608. [[CrossRef](#)]
7. Zhou, L.T.; Zhang, W.K.; Wang, Y.F.; Liang, S.; Gan, Y.P.; Huang, H.; Zhang, J.; Xia, Y.; Liang, C. Lithium Sulfide as Cathode Materials for Lithium-Ion Batteries: Advances and Challenges. *J. Chem.* **2020**, *2020*, 17. [[CrossRef](#)]
8. Stenzel, Y.; Horsthemke, F.; Winter, M.; Nowak, S. Chromatographic Techniques in the Research Area of Lithium Ion Batteries: Current State-of-the-Art. *Separations* **2019**, *6*, 26. [[CrossRef](#)]
9. Long, J.J.; Yu, H.; Liu, W.B. Structure engineering of cathode host materials for Li-S batteries. *Rare Met.* **2024**, *43*, 1370–1389. [[CrossRef](#)]
10. Goodenough, J.B.; Park, K.S. The Li-ion rechargeable battery: A perspective. *J. Am. Chem. Soc.* **2013**, *135*, 1167–1176. [[CrossRef](#)]
11. Manthiram, A. A reflection on lithium-ion battery cathode chemistry. *Nat. Commun.* **2020**, *11*, 1550. [[CrossRef](#)] [[PubMed](#)]
12. Golubkov, A.W.; Fuchs, D.; Wagner, J.; Wiltsche, H.; Stangl, C.; Fauler, G.; Voitic, G.; Thaler, A.; Hacker, V. Thermal-runaway experiments on consumer Li-ion batteries with metal-oxide and olivin-type cathodes. *RSC Adv.* **2014**, *4*, 3633–3642. [[CrossRef](#)]

13. Luo, R.; Wang, C.; Zhang, Z.; Lv, W.; Wei, Z.; Zhang, Y.; Luo, X.; He, W. Three-Dimensional Nanoporous Polyethylene-Reinforced PVDF-HFP Separator Enabled by Dual-Solvent Hierarchical Gas Liberation for Ultrahigh-Rate Lithium Ion Batteries. *Acs Appl. Energy Mater.* **2018**, *1*, 921–927. [[CrossRef](#)]
14. Kong, W.; Li, H.; Huang, X.; Chen, L. Gas evolution behaviors for several cathode materials in lithium-ion batteries. *J. Power Sources* **2005**, *142*, 285–291. [[CrossRef](#)]
15. Jung, R.; Metzger, M.; Maglia, F.; Stinner, C.; Gasteiger, H.A. Oxygen Release and Its Effect on the Cycling Stability of $\text{LiNi}_x\text{Mn}_y\text{Co}_z\text{O}_2$ (NMC) Cathode Materials for Li-Ion Batteries. *J. Electrochem. Soc.* **2017**, *164*, A1361–A1377. [[CrossRef](#)]
16. Self, J.; Aiken, C.P.; Petibon, R.; Dahn, J.R. Survey of Gas Expansion in Li-Ion NMC Pouch Cells. *J. Electrochem. Soc.* **2015**, *162*, A796–A802. [[CrossRef](#)]
17. Berkes, B.B.; Jozwiuk, A.; Vračar, M.; Sommer, H.; Brezesinski, T.; Janek, J. Online Continuous Flow Differential Electrochemical Mass Spectrometry with a Realistic Battery Setup for High-Precision, Long-Term Cycling Tests. *Anal. Chem.* **2015**, *87*, 5878–5883. [[CrossRef](#)]
18. Wandt, J.; Freiberg, A.T.S.; Ogrodnik, A.; Gasteiger, H.A. Singlet oxygen evolution from layered transition metal oxide cathode materials and its implications for lithium-ion batteries. *Mater. Today* **2018**, *21*, 825–833. [[CrossRef](#)]
19. Geng, L.; Liu, J.; Wood, D.L.; Qin, Y.; Lu, W.; Jafta, C.J.; Bai, Y.; Belharouak, I. Probing Thermal Stability of Li-Ion Battery Ni-Rich Layered Oxide Cathodes by means of Operando Gas Analysis and Neutron Diffraction. *ACS Appl. Energy Mater.* **2020**, *3*, 7058–7065. [[CrossRef](#)]
20. Wu, N.; Shen, J.; Zhou, X.; Li, S.; Li, J.; Liu, G.; Guo, D.; Deng, W.; Yuan, C.; Liu, X.; et al. Constructing Iron Vacancies in Thiospinel FeIn_2S_4 to Modulate Fe D-Band Center and Accelerate Sodiation Kinetics Enabling High-Rate and Durable Sodium Storage. *Adv. Energy Mater.* **2025**, *2025*, 2405729. [[CrossRef](#)]
21. Back, C.K.; Yin, R.-Z.; Shin, S.-J.; Lee, Y.-S.; Choi, W.; Kim, Y.-S. Electrochemical Properties and Gas Evolution Behavior of Overlithiated Li_2NiO_2 as Cathode Active Mass for Rechargeable Li Ion Batteries. *J. Electrochem. Soc.* **2012**, *159*, A887–A893. [[CrossRef](#)]
22. Belharouak, I.; Koenig, G.M.; Tan, T.; Yumoto, H.; Ota, N.; Amine, K. Performance Degradation and Gassing of $\text{Li}_4\text{Ti}_5\text{O}_{12}/\text{LiMn}_2\text{O}_4$ Lithium-Ion Cells. *J. Electrochem. Soc.* **2012**, *159*, A1165–A1170. [[CrossRef](#)]
23. Belharouak, I.; Koenig, G.M.; Amine, K. Electrochemistry and safety of $\text{Li}_4\text{Ti}_5\text{O}_{12}$ and graphite anodes paired with LiMn_2O_4 for hybrid electric vehicle Li-ion battery applications. *J. Power Sources* **2011**, *196*, 10344–10350. [[CrossRef](#)]
24. Golubkov, A.W.; Scheikl, S.; Planteu, R.; Voitic, G.; Wiltsche, H.; Stangl, C.; Fauler, G.; Thaler, A.; Hacker, V. Thermal runaway of commercial 18650 Li-ion batteries with LFP and NCA cathodes—Impact of state of charge and overcharge. *RSC Adv.* **2015**, *5*, 57171–57186. [[CrossRef](#)]
25. Lee, Y.K. Effect of transition metal ions on solid electrolyte interphase layer on the graphite electrode in lithium ion battery. *J. Power Sources* **2021**, *484*, 229270. [[CrossRef](#)]
26. Shin, H.; Park, J.; Sastry, A.M.; Lu, W. Degradation of the solid electrolyte interphase induced by the deposition of manganese ions. *J. Power Sources* **2015**, *284*, 416–427. [[CrossRef](#)]
27. Xie, Y.; Li, W.; Hu, H.; Shi, C.-G.; Hong, Y.-H.; Dai, P.; Lin, Z.; Sha, Y.; Wang, J.; Xie, L.; et al. Unraveling the Roles of Dissolved $\text{Mn}^{(2+)}$ and Its Impact on the Electrode–Electrolyte Interface under Realistic Conditions. *ACS Sustain. Chem. Eng.* **2024**, *12*, 6529–6538. [[CrossRef](#)]
28. Zhao, Q.-f.; Yu, Y.-h.; Ouyang, Q.-s.; Hu, M.-y.; Wang, C.; Ge, J.-h.; Zhang, S.-q.; Jiang, G.-h. Surface modification of LiFePO_4 by Coatings for Improving of Lithium-ion Battery Properties. *Int. J. Electrochem. Sci.* **2022**, *17*, 221142. [[CrossRef](#)]
29. Harold, U.; Escobar-Hernandez, R.M.G.; Papadaki, M.I.; Sachdeva, S.; Mannan, M.S. Thermal Runaway in Lithium-Ion Batteries: Incidents, Kinetics of the Runaway and Assessment of Factors Affecting Its Initiation. *J. Electrochem. Soc.* **2016**, *163*, A2691–A2701.
30. Zhang, Y.; Wang, H.; Yu, H.; Jia, T.; Ma, C. Influence of Cathode Materials on the Characteristics of Lithium-Ion Battery Gas Generation During Thermal Runaway. *Fire Technol.* **2024**. [[CrossRef](#)]
31. Chen, J.; Xu, C.; Wang, Q.; Wang, H.; Peng, Y.; Liu, J.; Zhang, J.; Zhang, G.; Lu, L.; Feng, X. The thermal-gas coupling mechanism of lithium iron phosphate batteries during thermal runaway. *J. Power Sources* **2025**, *625*, 235728. [[CrossRef](#)]
32. Zhang, H.; Xue, J.; Qin, Y.; Chen, J.; Wang, J.; Yu, X.; Zhang, B.; Zou, Y.; Hong, Y.H.; Li, Z.; et al. Full-Dimensional Analysis of Gaseous Products to Unlocking In Depth Thermal Runaway Mechanism of Li-Ion Batteries. *Small* **2024**, *20*, e2406110. [[CrossRef](#)] [[PubMed](#)]
33. Jia, Z.; Qin, P.; Li, Z.; Wei, Z.; Jin, K.; Jiang, L.; Wang, Q. Analysis of gas release during the process of thermal runaway of lithium-ion batteries with three different cathode materials. *J. Energy Storage* **2022**, *50*, 104302. [[CrossRef](#)]
34. Dong, T.; Xu, G.; Xie, B.; Liu, T.; Gong, T.; Sun, C.; Wang, J.; Zhang, S.; Zhang, X.; Zhang, H.; et al. An Electrode-Crosstalk-Suppressing Smart Polymer Electrolyte for High Safety Lithium-Ion Batteries. *Adv. Mater.* **2024**, *36*, 2400737. [[CrossRef](#)]
35. Zhou, Y.M.; Wang, P.Y.; Wang, K.; Fang, X.D.; Li, W.; Nai, J.; Liu, Y.J.; Wang, Y.; Zou, S.H.; Yuan, H.D.; et al. Developing High-Performance Anode-Free Lithium Batteries: Challenges, Strategies, and Opportunities. *Adv. Funct. Mater.* **2025**, *30*, 2424022. [[CrossRef](#)]

36. Zhao, H.J.; Deng, N.P.; Yan, J.; Kang, W.M.; Ju, J.G.; Ruan, Y.L.; Wang, X.Q.; Zhuang, X.P.; Li, Q.X.; Cheng, B.W. A review on anode for lithium-sulfur batteries: Progress and prospects. *Chem. Eng. J.* **2018**, *347*, 343–365. [[CrossRef](#)]
37. Yi, X.P.; Qi, G.Q.; Liu, X.L.; Depcik, C.; Liu, L. Challenges and strategies toward anode materials with different lithium storage mechanisms for rechargeable lithium batteries. *J. Energy Storage* **2024**, *95*, 23. [[CrossRef](#)]
38. Shen, Z.; Huang, J.; Xie, Y.; Wei, D.; Chen, J.; Shi, Z. Solid Electrolyte Interphase on Lithium Metal Anodes. *ChemSusChem* **2024**, *17*, e202301777. [[CrossRef](#)]
39. Kim, M.; You, H.M.; Jeon, J.; Lim, J.; Han, Y.; Kim, K.; Hong, J. Thermal decomposition mechanism of lithium methyl carbonate in solid electrolyte interphase layer of lithium-ion battery. *Energy Storage Mater.* **2024**, *70*, 103517. [[CrossRef](#)]
40. Parimalam, B.S.; MacIntosh, A.D.; Kadam, R.; Lucht, B.L. Decomposition Reactions of Anode Solid Electrolyte Interphase (SEI) Components with LiPF₆. *J. Phys. Chem. C* **2017**, *121*, 22733–22738. [[CrossRef](#)]
41. Wu, J.; Weng, S.; Zhang, X.; Sun, W.; Wu, W.; Wang, Q.; Yu, X.; Chen, L.; Wang, Z.; Wang, X. In Situ Detecting Thermal Stability of Solid Electrolyte Interphase (SEI). *Small* **2023**, *19*, e2208239. [[CrossRef](#)]
42. Wu, N.; He, W.; Shi, S.; Yuan, X.; Li, J.; Cao, J.; Yuan, C.; Liu, X. Bamboo fiber-derived carbon support for the immobilization of Pt nanoparticles to enhance hydrogen evolution reaction. *J. Colloid Interface Sci.* **2025**, *684*, 658–667. [[CrossRef](#)] [[PubMed](#)]
43. Liu, X.; Yin, L.; Ren, D.; Wang, L.; Ren, Y.; Xu, W.; Lapidus, S.; Wang, H.; He, X.; Chen, Z.; et al. In situ observation of thermal-driven degradation and safety concerns of lithiated graphite anode. *Nat. Commun.* **2021**, *12*, 4235. [[CrossRef](#)]
44. Fernandes, Y.; Bry, A.; de Persis, S. Identification and quantification of gases emitted during abuse tests by overcharge of a commercial Li-ion battery. *J. Power Sources* **2018**, *389*, 106–119. [[CrossRef](#)]
45. Bernhard, R.; Metzger, M.; Gasteiger, H.A. Gas Evolution at Graphite Anodes Depending on Electrolyte Water Content and SEI Quality Studied by On-Line Electrochemical Mass Spectrometry. *J. Electrochem. Soc.* **2015**, *162*, A1984–A1989. [[CrossRef](#)]
46. Michalak, B.; Sommer, H.; Mannes, D.; Kaestner, A.; Brezesinski, T.; Janek, J. Gas evolution in operating lithium-ion batteries studied in situ by neutron imaging. *Sci. Rep.* **2015**, *5*, 15627. [[CrossRef](#)] [[PubMed](#)]
47. Schwenke, K.U.; Solchenbach, S.; Demeaux, J.; Lucht, B.L.; Gasteiger, H.A. The Impact of CO₂ Evolved from VC and FEC during Formation of Graphite Anodes in Lithium-Ion Batteries. *J. Electrochem. Soc.* **2019**, *166*, A2035–A2047. [[CrossRef](#)]
48. Han, R.; Wang, Z.; Huang, D.; Zhang, F.; Pan, A.; Song, H.; Wei, Y.; Liu, Y.; Wang, L.; Li, Y.; et al. High-Energy-Density Lithium Metal Batteries with Impressive Li(+) Transport Dynamic and Wide-Temperature Performance from –60 to 60 degrees C. *Small* **2023**, *19*, e2300571. [[CrossRef](#)] [[PubMed](#)]
49. Zhang, H.; Wu, X.; Li, Z.; Zou, Y.; Wang, J.; Yu, X.; Chen, J.; Xue, J.; Zhang, B.; Tian, J.H.; et al. Full-Dimensional Analysis of Gaseous Products Within Li-Ion Batteries by On-Line GC-BID/MS. *Adv. Energy Mater.* **2024**, *14*, 2400397. [[CrossRef](#)]
50. Huang, Y.; Yang, H.; Gao, Y.; Chen, G.; Li, Y.; Shi, L.; Zhang, D. Mechanism and solutions of lithium dendrite growth in lithium metal batteries. *Mater. Chem. Front.* **2024**, *8*, 1282–1299. [[CrossRef](#)]
51. Wang, S.; Rafiz, K.; Liu, J.; Jin, Y.; Lin, J.Y.S. Effects of lithium dendrites on thermal runaway and gassing of LiFePO₄ batteries. *Sustain. Energy Fuels* **2020**, *4*, 2342–2351. [[CrossRef](#)]
52. Zhang, G.; Wei, X.; Han, G.; Dai, H.; Zhu, J.; Wang, X.; Tang, X.; Ye, J. Lithium plating on the anode for lithium-ion batteries during long-term low temperature cycling. *J. Power Sources* **2021**, *484*, 229312. [[CrossRef](#)]
53. Berckmans, G.; De Sutter, L.; Kersys, A.; Kriston, A.; Marinaro, M.; Kasper, M.; Axmann, P.; Smekens, J.; Wohlfahrt-Mehrens, M.; Pfrang, A.; et al. Electrical Characterization and Micro X-ray Computed Tomography Analysis of Next-Generation Silicon Alloy Lithium-Ion Cells. *World Electr. Veh. J.* **2018**, *9*, 43. [[CrossRef](#)]
54. Zhang, L.Q.; Zhu, C.X.; Yu, S.C.; Ge, D.H.; Zhou, H.S. Status and challenges facing representative anode materials for rechargeable lithium batteries. *J. Energy Chem.* **2022**, *66*, 260–294. [[CrossRef](#)]
55. Khan, M.; Yan, S.; Ali, M.; Mahmood, F.; Zheng, Y.; Li, G.; Liu, J.; Song, X.; Wang, Y. Innovative Solutions for High-Performance Silicon Anodes in Lithium-Ion Batteries: Overcoming Challenges and Real-World Applications. *Nanomicro Lett.* **2024**, *16*, 179. [[CrossRef](#)]
56. Sun, Y.; Liu, K.; Zhu, Y. Recent Progress in Synthesis and Application of Low-Dimensional Silicon Based Anode Material for Lithium Ion Battery. *J. Nanomater.* **2017**, *2017*, 1–15. [[CrossRef](#)]
57. Shen, X.; Liu, H.; Cheng, X.-B.; Yan, C.; Huang, J.-Q. Beyond lithium ion batteries: Higher energy density battery systems based on lithium metal anodes. *Energy Storage Mater.* **2018**, *12*, 161–175. [[CrossRef](#)]
58. Gao, Y.; Guo, M.; Yuan, K.; Shen, C.; Ren, Z.; Zhang, K.; Zhao, H.; Qiao, F.; Gu, J.; Qi, Y.; et al. Multifunctional Silanization Interface for High-Energy and Low-Gassing Lithium Metal Pouch Cells. *Adv. Energy Mater.* **2019**, *10*, 1903362. [[CrossRef](#)]
59. Peng, Y.; Ding, M.; Zhang, K.; Zhang, H.; Hu, Y.; Lin, Y.; Hu, W.; Liao, Y.; Tang, S.; Liang, J.; et al. Quantitative Analysis of the Coupled Mechanisms of Lithium Plating, SEI Growth, and Electrolyte Decomposition in Fast Charging Battery. *ACS Energy Lett.* **2024**, *9*, 6022–6028. [[CrossRef](#)]
60. Zhao, H.; Wang, J.; Shao, H.; Xu, K.; Deng, Y. Gas Generation Mechanism in Li-Metal Batteries. *Energy Environ. Mater.* **2021**, *5*, 327–336. [[CrossRef](#)]

61. Etxebarria, A.; Yun, D.-J.; Blum, M.; Ye, Y.; Sun, M.; Lee, K.-J.; Su, H.; Muñoz-Márquez, M.Á.; Ross, P.N.; Crumlin, E.J. Revealing In Situ Li Metal Anode Surface Evolution upon Exposure to CO₂ Using Ambient Pressure X-Ray Photoelectron Spectroscopy. *ACS Appl. Mater. Interfaces* **2020**, *12*, 26607–26613. [CrossRef] [PubMed]
62. Chen, X.; Hou, T.-Z.; Li, B.; Yan, C.; Zhu, L.; Guan, C.; Cheng, X.-B.; Peng, H.-J.; Huang, J.-Q.; Zhang, Q. Towards stable lithium-sulfur batteries: Mechanistic insights into electrolyte decomposition on lithium metal anode. *Energy Storage Mater.* **2017**, *8*, 194–201. [CrossRef]
63. Nagar, A.; Garg, A.; Singh, S.; Gao, L.; Kim, J.; Wei, K. Reactive Force Field (ReaxFF) and Universal Force Field Molecular Dynamic Simulation of Solid Electrolyte Interphase Components in Lithium-Ion Batteries. *J. Electrochem. Energy Convers. Storage* **2024**, *21*, 021006. [CrossRef]
64. Jo, S.; Seo, S.; Kang, S.K.; Na, I.; Kunze, S.; Song, M.; Hwang, S.; Woo, S.P.; Kim, S.; Kim, W.B.; et al. Thermal Runaway Mechanism in Ni-Rich Cathode Full Cells of Lithium-Ion Batteries: The Role of Multidirectional Crosstalk. *Adv. Mater.* **2024**, *36*, e2402024. [CrossRef]
65. He, Y.-B.; Li, B.; Liu, M.; Zhang, C.; Lv, W.; Yang, C.; Li, J.; Du, H.; Zhang, B.; Yang, Q.-H.; et al. Gassing in Li₄Ti₅O₁₂-based batteries and its remedy. *Sci. Rep.* **2012**, *2*, 913. [CrossRef]
66. Hu, Q.; He, Y.; Ren, D.; Song, Y.; Wu, Y.; Liang, H.; Gao, J.; Xu, G.; Cai, J.; Li, T.; et al. Targeted masking enables stable cycling of LiNi_{0.6}Co_{0.2}Mn_{0.2}O₂ at 4.6V. *Nano Energy* **2022**, *96*, 107123. [CrossRef]
67. Mu, X.W.; Ding, H.L.; Wu, Y.D.; Hu, H.B.; Yu, B. Nonflammable Liquid Electrolytes for Safe Lithium Batteries. *Small Struct.* **2023**, *4*, 13. [CrossRef]
68. Xu, G.J.; Shangguan, X.H.; Dong, S.M.; Zhou, X.H.; Cui, G.L. Formulation of Blended-Lithium-Salt Electrolytes for Lithium Batteries. *Angew. Chem.-Int. Ed.* **2020**, *59*, 3400–3415. [CrossRef]
69. Zhou, G.; Niu, C.; Kong, Y.; Wei, Z.; Wang, J.; Huang, Q.; Lu, H.; Zhang, Q. Research on stimulation responsive electrolytes from the perspective of thermal runaway in lithium-ion batteries: A review. *Fuel* **2024**, *368*, 131599. [CrossRef]
70. Han, Z.; Zhang, D.; Wang, H.; Zheng, G.; Liu, M.; He, Y. Research Progress and Prospect on Electrolyte Additives for Interface Reconstruction of Long-Life Ni-Rich Lithium Batteries. *Acta Phys.-Chim. Sin.* **2024**, *40*, 2307034. [CrossRef]
71. Kriston, A.; Adanouj, I.; Ruiz, V.; Pfrang, A. Quantification and simulation of thermal decomposition reactions of Li-ion battery materials by simultaneous thermal analysis coupled with gas analysis. *J. Power Sources* **2019**, *435*, 226774. [CrossRef]
72. Schmitz, R.W.; Murmann, P.; Schmitz, R.; Müller, R.; Krämer, L.; Kasnatscheew, J.; Isken, P.; Niehoff, P.; Nowak, S.; Röschen-thaler, G.-V.; et al. Investigations on novel electrolytes, solvents and SEI additives for use in lithium-ion batteries: Systematic electrochemical characterization and detailed analysis by spectroscopic methods. *Prog. Solid State Chem.* **2014**, *42*, 65–84. [CrossRef]
73. Inamoto, J.-I.; Fukutsuka, T.; Miyazaki, K.; Abe, T. Investigation on Surface-Film Formation Behavior of LiMn₂O₄ Thin-Film Electrodes in LiClO₄/Propylene Carbonate. *ChemistrySelect* **2017**, *2*, 2895–2900. [CrossRef]
74. Wang, C.; Zhang, H.; Li, J.; Chai, J.; Dong, S.; Cui, G. The interfacial evolution between polycarbonate-based polymer electrolyte and Li-metal anode. *J. Power Sources* **2018**, *397*, 157–161. [CrossRef]
75. Liao, Z.; Zhang, S.; Zhao, Y.; Qiu, Z.; Li, K.; Han, D.; Zhang, G.; Haberle, T.G. Experimental evaluation of thermolysis-driven gas emissions from LiPF₆-carbonate electrolyte used in lithium-ion batteries. *J. Energy Chem.* **2020**, *49*, 124–135. [CrossRef]
76. Liu, Y.M.; Nicolau, B.G.; Esbensen, J.L.; Gewirth, A.A. Characterization of the Cathode Electrolyte Interface in Lithium Ion Batteries by Desorption Electrospray Ionization Mass Spectrometry. *Anal. Chem.* **2016**, *88*, 7171–7177. [CrossRef] [PubMed]
77. Melin, T.; Lundström, R.; Berg, E.J. Revisiting the Ethylene Carbonate–Propylene Carbonate Mystery with Operando Characterization. *Adv. Mater. Interfaces* **2021**, *9*, 2101258. [CrossRef]
78. Yang, H.; Zhuang, G.V.; Ross, P.N. Thermal stability of LiPF₆ salt and Li-ion battery electrolytes containing LiPF₆. *J. Power Sources* **2006**, *161*, 573–579. [CrossRef]
79. Liao, Y.; Zhang, H.; Peng, Y.; Hu, Y.; Liang, J.; Gong, Z.; Wei, Y.; Yang, Y. Electrolyte Degradation During Aging Process of Lithium-Ion Batteries: Mechanisms, Characterization, and Quantitative Analysis. *Adv. Energy Mater.* **2024**, *14*, 2304295. [CrossRef]
80. Ortiz, D.; Steinmetz, V.; Durand, D.; Legand, S.; Dauvois, V.; Maitre, P.; Le Caer, S. Radiolysis as a solution for accelerated ageing studies of electrolytes in Lithium-ion batteries. *Nat. Commun.* **2015**, *6*, 6950. [CrossRef]
81. Liu, P.; Yang, L.; Xiao, B.; Wang, H.; Li, L.; Ye, S.; Li, Y.; Ren, X.; Ouyang, X.; Hu, J.; et al. Revealing Lithium Battery Gas Generation for Safer Practical Applications. *Adv. Funct. Mater.* **2022**, *32*, 2208586. [CrossRef]
82. Han, J.G.; Kim, K.; Lee, Y.; Choi, N.S. Scavenging Materials to Stabilize LiPF(6) -Containing Carbonate-Based Electrolytes for Li-Ion Batteries. *Adv. Mater.* **2019**, *31*, e1804822. [CrossRef] [PubMed]
83. Tebbe, J.L.; Fuerst, T.F.; Musgrave, C.B. Mechanism of hydrofluoric acid formation in ethylene carbonate electrolytes with fluorine salt additives. *J. Power Sources* **2015**, *297*, 427–435. [CrossRef]
84. Larsson, F.; Andersson, P.; Blomqvist, P.; Mellander, B.E. Toxic fluoride gas emissions from lithium-ion battery fires. *Sci. Rep.* **2017**, *7*, 10018. [CrossRef]

85. Agubra, V.A.; Fergus, J.W. The formation and stability of the solid electrolyte interface on the graphite anode. *J. Power Sources* **2014**, *268*, 153–162. [CrossRef]
86. Wu, J.; Liu, S.; Han, F.; Yao, X.; Wang, C. Lithium/Sulfide All-Solid-State Batteries using Sulfide Electrolytes. *Adv. Mater.* **2021**, *33*, e2000751. [CrossRef]
87. Wu, N.; Zhao, Z.; Zhang, Y.; Hua, R.; Li, J.; Liu, G.; Guo, D.; Zhao, J.; Cao, A.; Sun, G.; et al. Revealing the fast reaction kinetics and interfacial behaviors of CuFeS₂ hollow nanorods for durable and high-rate sodium storage. *J. Colloid Interface Sci.* **2025**, *679*, 990–1000. [CrossRef] [PubMed]
88. Ito, A.; Kimura, T.; Sakuda, A.; Tatsumisago, M.; Hayashi, A. Liquid-phase synthesis of Li₃PS₄ solid electrolyte using ethylenediamine. *J. Sol-Gel Sci. Technol.* **2021**, *101*, 2–7. [CrossRef]
89. Yersak, T.A.; Gonzalez Malabet, H.J.; Yadav, V.; Pieczonka, N.P.W.; Collin, W.; Cai, M. Flammability of sulfide solid-state electrolytes β -Li₃PS₄ and Li₆PS₅Cl: Volatilization and autoignition of sulfur vapor—New insight into all-solid-state battery thermal runaway. *J. Energy Chem.* **2025**, *102*, 651–660. [CrossRef]
90. Lee, E.; Kim, H.; Choi, H.; Kim, S.Y.; Chung, K.Y. Unraveling the reversible redox mechanism of Li₍₆₎PS₍₅₎Cl solid electrolyte in all-solid-state lithium-sulfur batteries. *Chem. Commun.* **2024**, *60*, 14834–14837. [CrossRef]
91. Nikodimos, Y.; Huang, C.-J.; Taklu, B.W.; Su, W.-N.; Hwang, B.J. Chemical stability of sulfide solid-state electrolytes: Stability toward humid air and compatibility with solvents and binders. *Energy Environ. Sci.* **2022**, *15*, 991–1033. [CrossRef]
92. Lu, P.; Liu, L.; Wang, S.; Xu, J.; Peng, J.; Yan, W.; Wang, Q.; Li, H.; Chen, L.; Wu, F. Superior All-Solid-State Batteries Enabled by a Gas-Phase-Synthesized Sulfide Electrolyte with Ultrahigh Moisture Stability and Ionic Conductivity. *Adv. Mater.* **2021**, *33*, 2100921. [CrossRef] [PubMed]
93. Sun, Y.Z.; Huang, J.Q.; Zhao, C.Z.; Zhang, Q. A review of solid electrolytes for safe lithium-sulfur batteries. *Sci. China-Chem.* **2017**, *60*, 1508–1526. [CrossRef]
94. Takada, K. Progress in solid electrolytes toward realizing solid-state lithium batteries. *J. Power Sources* **2018**, *394*, 74–85. [CrossRef]
95. Indu, M.S.; Alexander, G.V.; Sreejith, O.V.; Abraham, S.E.; Murugan, R. Lithium garnet-cathode interfacial chemistry: Inclusive insights and outlook toward practical solid-state lithium metal batteries. *Mater. Today Energy* **2021**, *21*, 46. [CrossRef]
96. Hou, W.; Ou, Y.; Liu, K. Progress on High Voltage PEO-based Polymer Solid Electrolytes in Lithium Batteries. *Chem. Res. Chin. Univ.* **2022**, *38*, 735–743. [CrossRef]
97. Hubble, D.; Brown, D.E.; Zhao, Y.; Fang, C.; Lau, J.; McCloskey, B.D.; Liu, G. Liquid electrolyte development for low-temperature lithium-ion batteries. *Energy Environ. Sci.* **2022**, *15*, 550–578. [CrossRef]
98. Wang, C.; Yang, Y.; Liu, X.; Zhong, H.; Xu, H.; Xu, Z.; Shao, H.; Ding, F. Suppression of Lithium Dendrite Formation by Using LAGP-PEO (LiTFSI) Composite Solid Electrolyte and Lithium Metal Anode Modified by PEO (LiTFSI) in All-Solid-State Lithium Batteries. *ACS Appl. Mater. Interfaces* **2017**, *9*, 13694–13702. [CrossRef] [PubMed]
99. Yi, M.; Li, J.; Wang, M.; Fan, X.; Hong, B.; Zhang, Z.; Zhang, Z.; Jiang, H.; Wang, A.; Lai, Y. Suppressing structural degradation of single crystal nickel-rich cathodes in PEO-based all-solid-state batteries: Mechanistic insight and performance. *Energy Storage Mater.* **2023**, *54*, 579–588. [CrossRef]
100. Nie, K.; Wang, X.; Qiu, J.; Wang, Y.; Yang, Q.; Xu, J.; Yu, X.; Li, H.; Huang, X.; Chen, L. Increasing Poly(ethylene oxide) Stability to 4.5 V by Surface Coating of the Cathode. *ACS Energy Lett.* **2020**, *5*, 826–832. [CrossRef]
101. Barbosa, J.C.; Dias, J.P.; Lanceros-Mendez, S.; Costa, C.M. Recent Advances in Poly(vinylidene fluoride) and Its Copolymers for Lithium-Ion Battery Separators. *Membranes* **2018**, *8*, 45. [CrossRef] [PubMed]
102. Song, L.; Xiong, Y.; Xiao, Z.; Li, A.; Yan, L.; Kuang, Y.; Zhao, T. Research progress on the mechanism and key role of filler structure on properties of PVDF composite solid electrolyte. *Ionics* **2024**, *30*, 5861–5877. [CrossRef]
103. Jin, Y.; Zheng, Z.; Wei, D.; Jiang, X.; Lu, H.; Sun, L.; Tao, F.; Guo, D.; Liu, Y.; Gao, J.; et al. Detection of Micro-Scale Li Dendrite via H₂ Gas Capture for Early Safety Warning. *Joule* **2020**, *4*, 1714–1729. [CrossRef]
104. Fell, C.R.; Sun, L.; Hallac, P.B.; Metz, B.; Sisk, B. Investigation of the Gas Generation in Lithium Titanate Anode Based Lithium Ion Batteries. *J. Electrochem. Soc.* **2015**, *162*, A1916–A1920. [CrossRef]
105. Wu, Y.; Liu, X.; Wang, L.; Feng, X.; Ren, D.; Li, Y.; Rui, X.; Wang, Y.; Han, X.; Xu, G.-L.; et al. Development of cathode-electrolyte-interphase for safer lithium batteries. *Energy Storage Mater.* **2021**, *37*, 77–86. [CrossRef]
106. Guo, X.-X.; Li, Y.-Q.; Cui, Z.-H.; Rui, F.; Ning, Z.; Du, F.-M. Influence of Electronic Conducting Additives on Cycle Performance of Garnet-based Solid Lithium Batteries. *J. Inorg. Mater.* **2018**, *33*, 462–470.
107. Metzger, M.; Marino, C.; Sicklinger, J.; Haering, D.; Gasteiger, H.A. Anodic Oxidation of Conductive Carbon and Ethylene Carbonate in High-Voltage Li-Ion Batteries Quantified by On-Line Electrochemical Mass Spectrometry. *J. Electrochem. Soc.* **2015**, *162*, A1123–A1134. [CrossRef]
108. Metzger, M.; Sicklinger, J.; Haering, D.; Kavakli, C.; Stinner, C.; Marino, C.; Gasteiger, H.A. Carbon Coating Stability on High-Voltage Cathode Materials in H₂O-Free and H₂O-Containing Electrolyte. *J. Electrochem. Soc.* **2015**, *162*, A1227–A1235. [CrossRef]

109. Kajiyama, A.; Masaki, R.; Wakiyama, T.; Matsumoto, K.; Yoda, A.; Inada, T.; Yokota, H.; Kanno, R. Principal Factors of Carbon Conductive Agents that Contribute to the Gas Formation in High-Voltage Cathode Systems. *J. Electrochem. Soc.* **2015**, *162*, A1516–A1522. [[CrossRef](#)]
110. Salomez, B.; Gruegeon, S.; Armand, M.; Tran-Van, P.; Laruelle, S. Review—Gassing Mechanisms in Lithium-ion Battery. *J. Electrochem. Soc.* **2023**, *170*, 050537. [[CrossRef](#)]
111. Renfrew, S.E.; McCloskey, B.D. Residual Lithium Carbonate Predominantly Accounts for First Cycle CO₂ and CO Outgassing of Li-Stoichiometric and Li-Rich Layered Transition-Metal Oxides. *J. Am. Chem. Soc.* **2017**, *139*, 17853–17860. [[CrossRef](#)] [[PubMed](#)]
112. Mahne, N.; Renfrew, S.E.; McCloskey, B.D.; Freunberger, S.A. Electrochemical Oxidation of Lithium Carbonate Generates Singlet Oxygen. *Angew. Chem. Int. Ed.* **2018**, *57*, 5529–5533. [[CrossRef](#)] [[PubMed](#)]
113. Zhuang, X.; Zhang, S.; Cui, Z.; Xie, B.; Gong, T.; Zhang, X.; Li, J.; Wu, R.; Wang, S.; Qiao, L.; et al. Interphase Regulation by Multifunctional Additive Empowering High Energy Lithium-Ion Batteries with Enhanced Cycle Life and Thermal Safety. *Angew. Chem. Int. Ed.* **2023**, *63*, e202315710. [[CrossRef](#)]
114. Sun, J.; Chen, G.; Wang, B.; Li, J.; Xu, G.; Wu, T.; Tang, Y.; Dong, S.; Huang, J.; Cui, G. Lithium Hydride in the Solid Electrolyte Interphase of Lithium-Ion Batteries as a Pulverization Accelerator of Silicon. *Angew. Chem. Int. Ed.* **2024**, *63*, e202406198. [[CrossRef](#)]
115. Wang, Q.; Ping, P.; Zhao, X.; Chu, G.; Sun, J.; Chen, C. Thermal runaway caused fire and explosion of lithium ion battery. *J. Power Sources* **2012**, *208*, 210–224. [[CrossRef](#)]
116. Wang, Z.; He, T.; Bian, H.; Jiang, F.; Yang, Y. Characteristics of and factors influencing thermal runaway propagation in lithium-ion battery packs. *J. Energy Storage* **2021**, *41*, 102956. [[CrossRef](#)]
117. Zhang, X.; Yao, J.; Zhu, L.; Wu, J.; Wei, D.; Wang, Q.; Chen, H.; Li, K.; Gao, Z.; Xu, C.; et al. Experimental and simulation investigation of thermal runaway propagation in lithium-ion battery pack systems. *J. Energy Storage* **2024**, *77*, 109868. [[CrossRef](#)]

Disclaimer/Publisher's Note: The statements, opinions and data contained in all publications are solely those of the individual author(s) and contributor(s) and not of MDPI and/or the editor(s). MDPI and/or the editor(s) disclaim responsibility for any injury to people or property resulting from any ideas, methods, instructions or products referred to in the content.